5-18-2023

Emergent Properties of Cells and Tissues in Health and Disease

Pancy T. Lwin
ptl1411@rit.edu

Recommended Citation

Lwin, Pancy T., "Emergent Properties of Cells and Tissues in Health and Disease" (2023). Thesis. Rochester Institute of Technology. Accessed from

Emergent properties of cells and tissues in health and disease

Ph.D. Degree Dissertation

Pancy T. Lwin

May 18, 2023

Rochester Institute of Technology
College of Science
School of Mathematical Sciences

Submitted in Partial Fulfillment of the Requirements in
Mathematical Modeling PhD Program

Dr. Moumita Das 05/05/2023

School of Physics and Astronomy

Rochester Institute of Technology

Dissertation Advisor

Dr. André Hudson 05/05/2023

Thomas H. Gosnell School of Life Sciences

Rochester Institute of Technology

Chair of Dissertation Committee

Dr. Lishibanya Mohapatra 05/05/2023

School of Physics and Astronomy

Rochester Institute of Technology

Dissertation Committee Member

Dr. Michael Cromer 05/05/2023

School of Mathematical Sciences

Rochester Institute of Technology

Dissertation Committee Member

Dr. Jennifer M. Schwarz 05/05/2023

College of Arts and Sciences

Biophysical Science

Syracuse University

Dissertation Committee Member

Contents

1 Introduction 11

1.1 Motivation 11

1.2 Outline 12

2 Mechanics of Biopolymer Network in Tissues 17

2.1 Double Network System in Cartilage 17

2.2 Rigidity Percolation Theory 18

2.3 Model of Rigidly Percolating Double Network (RPDN) 21

2.4 Simulation Details 23

2.5 Calculation 26

2.5.1 Modulus and Stress 26

2.6 Results 30

2.7 Discussion 33

2.7.1 Varying the inter-network interaction of the two networks . . . 33

2.7.2 Varying the ratio of filament stretching stiffness of the two networks 34

- 2.7.3 Varying the bond occupation probability of the stiff network . . 36
- 2.7.4 Understanding Tunability and Crack Propagation 37

2.8 Hysteresis Simulations 46

3 Mechanics of Biopolymer Network in Cells 55

3.1 Cytoskeleton Network 55

3.2 Model and Method of RPDN (motors) 56

- 3.2.1 Motor-Contracted Rigidly Percolating Double Network Model 56

3.3 Calculation 59

- 3.3.1 Bond Occupation Probability 59
- 3.3.2 Stretching and Bending Rigidity 60
- 3.3.3 Contractility 62

3.4 Results 63

3.5 Discussion 64

4 Biophysics of Viral Life Cycle and the response to therapeutics 69

4.1 Viral Life Cycle 69

4.2 Results 76

- 4.2.1 Targeting Fecundity 76
- 4.2.2 Targeting Reproduction Rate 77
- 4.2.3 Targeting Infection Rate 78

4.3 Discussion 81

- 4.3.1 Simulation Details 85
- 4.3.2 Mathematical model (Details) 85

4.3.3 Administering Anti-viral Therapeutics 88
4.3.4 Meaning of extinction and time in the model 89
4.3.5 Targeting Fecundity (Details) 90
4.3.6 Targeting Reproduction Rate (Details) 91
4.3.7 Targeting Infection Rate (Details) 92

5 Conclusion 93

5.1 Conclusion 93

6 Future Work 95

6.1 Future Work I - Viscoelasticity of RPDN Model 95
6.2 Future Work II - Wound Healing Mechanism in Stentor Modeling . . 97
6.3 Future Work III - Living Biotic-Abiotic Materials with Temporally Programmable Actuation 97
6.4 Future Work IV - Virus Modeling 100

7 Acknowledgements 101

8 Glossary 105

Glossary 107

9 Bibliography 109

The waves of the sea, the little ripples on the shore, the sweeping curve of the sandy bay between the headlands, the outline of the hills, the shape of the clouds, all these are so many riddles of form, so many problems of morphology, and all of them the physicist can more or less easily read and adequately solve: solving them by reference to their antecedent phenomena, in the material system of mechanical forces to which they belong, and to which we interpret them as being due. They have also doubtless, their immanent teleological significance; but it is on another plane of thought from the physicist's that we contemplate their intrinsic harmony* and perfection, and "see that they are good."

D'Arcy Wentworth Thompson in *On Growth and Form*

Homo liber nulla de re minus quam de morte cogitat; et ejus sapientia non mortis sed vitae meditatio est.

Benedictus de Spinoza in *Ethics, Pt IV, Prop. 67.*

(There is nothing over which a free man ponders less than death; his wisdom is, to meditate not on death but on life.)

Erwin Schrödinger in *What is life?*

The mathematicians are well acquainted with the difference between pure science, which has to do only with ideas, and the application of its laws to the use of life, in which they are constrained to submit to the imperfections of matter and the influence of accident.

Dr Johnson in *the fourteenth Rambler*

Abstract

This dissertation uses statistical physics based mathematical models to investigate and predict the emergent properties of biological systems in both healthy and diseased states. Three projects are presented, each exploring a different aspect of biological systems.

The first project focuses on modeling cartilage-like tissue systems as a double network consisting of two interconnected networks. By using rigidity percolation theory, we study the tunable mechanics and fracture resistance of such biological tissues in healthy and degraded states. Our findings show that the secondary network density can be tuned to facilitate stress relaxation, leading to robust tissue properties when the primary network density is just above its rigidity percolation threshold. However, when the primary network is very dense, the double network becomes stiff and brittle. In the second project, we develop active double network models to investigate the interplay of actin-microtubule interactions and actomyosin dynamics in the cytoskeleton, an active network of proteins in cells. Our study reveals that the rigidity of the composite depends on the interplay between myosin-dependent crosslinking and contraction and the proximity of the actin or microtubule networks to the rigidity percolation threshold. The third project employs a viral quasispecies dynamics model to investigate the effectiveness of antiviral strategies that target different aspects of the lifecycle of cold or flu-like viruses, including COVID-19. Our results demonstrate that antivirals targeting fecundity and reproduction rates decrease the viral load linearly and via a power law, respectively. However, antivirals targeting

the infection rate cause a non-monotonic change in the viral load, initially increasing and then decreasing as the infection rate is decreased, particularly for individuals with low immunity.

In summary, the findings of these projects underscore the importance of understanding the underlying mechanisms behind the properties of biological cells and tissues. They also provide insights into the development of tunable, resilient, and adaptive biomaterials and the effectiveness of different antiviral strategies for COVID-19 and similar viral diseases.

Chapter 1

Introduction

1.1 Motivation

This dissertation aims to understand the mechanisms of tissues, cells, and viruses, not only in their healthy stages but also in their unhealthy or disease states, using statistical mechanics and mathematical modeling. Statistical mechanics is a broad field that uses probabilistic and statistical approaches to understand the emergent properties of meso- and macroscopic systems made of large collections of entities [45, 46]. Generally, a traditional statistical mechanics course covers a basic understanding of thermodynamics, ensemble theory, ideal gases, and phase transitions [68]. To understand and model the living world, Robbert Dijkgraaf, a theoretical physicist, stated in his article *To Solve the Biggest Mystery in Physics, Join Two Kinds of Law* [22] that we need to combine reductionism, a way of seeing in terms of elementary blocks, with emergence, complex laws arising from interactions among individual components. Biophysics applies the principles of physics to biological systems at the molecular, cellular, tissue, and organism scales.

In other words, just as thermodynamic laws emerge from the interactions among molecules, we may understand the working rules of biological systems by studying the mechanistic principles and interactions at play in biological systems. Emergent behavior can be defined as a collective phenomenon of working pieces, such as atoms in our work, fibers, and viruses. For example, we can understand the emergent and organizational structures of ant colonies when they float together and use that information to create a material that is buoyant, flexible, breathable, and waterproof [26]. Nigel Goldenfeld applied not only “biology to physics” but also “physics to biology” [12]. He provides an example of the collective behavior of bacteria and virus populations acting as condensed matter systems.

1.2 Outline

Our first project aims to model tissues, like cartilage, to understand both healthy and deteriorated stages. The second project models the collective restructuring feature of actin-microtubules with motors. The third project works on the infected state of the cell and compares the effectiveness of antiviral strategies in a viral life cycle - which is another emergent behavior of a quasispecies under therapeutics.

Composite fiber networks are ubiquitous in biological systems and synthetic materials with tunable and robust mechanical properties. For example, the cytoskeleton, the scaffolding that gives eukaryotic cells mechanical integrity and shape, is a self-organized composite network of protein filaments, including actin and microtubules [76]. The distinct rigidity of actin and microtubules enables cells to exhibit complex stress responses and architectures essential for a wide range of functions [24, 69, 79, 80]. Another prominent example of composite biopolymer networks is the extracellular matrix of musculoskeletal tissues like articular cartilage which is primarily made of networks of stiff collagen fibers which are responsible for resisting tension and a secondary network of brush-like proteoglycans and hyaluronic acid which interacts which reinforces the collagen network, and also helps to resist compression [101].

Finally, several synthetic double network hydrogels have recently emerged as extraordinarily robust materials with considerable toughness and fracture resistance compared to conventional single network hydrogels. For instance, the PAMPS-PAAm double network hydrogel, which consists of interacting networks of poly(2-acrylamide-2-methyl-propane sulfonic acid) and polyacrylamide, has a tearing energy $\sim 4400 J/m^2$, which is several hundred to a thousand times that of single network PAAm and PAMPS hydrogels[35, 66]. The exceptional mechanical response of these double network systems derives from the synergistic interplay between two networks with very different single-filament and collective properties. Therefore, in chapter 2, we study the mechanics and dynamics of biopolymer network in tissues with the aim of not only in the form of healthy and diseased cartilage and but also in the design principle of single versus double Network system described below.

The rigidity of stiff networks made of a single type of fiber or biopolymer, henceforth called single networks (SN), has been vigorously investigated in the past two decades, uncovering mechanical phase transitions, distinct mechanical regimes, and novel non-linear mechanical properties [6, 17, 30, 36, 39, 43, 61, 75, 82, 99]. More recently, studies of the fracture mechanics of such networks have demonstrated that low network connectivity and system-wide distribution of damage can provide protective mechanisms against failure [8, 104]. The mechanics and fracture of composite networks and materials, on the other hand, are only beginning to be explored theoretically, spanning systems such as composites materials made of rod-like inclusions in an SN [16, 18], composite networks [7], and continuum models of double network hydrogels [35]. The mechanical structure-function properties of Double Networks (DNs) [63, 88] are less well understood, and there remain many open questions as to the mechanisms by which DNs achieve such remarkable mechanical performance. In particular, it is unknown how much the second network can affect the rigidity percolation threshold for the combined DN system, an important parameter for setting the stiffness. Nor is it known to what degree the second network can tune the strain necessary for network failure (extensibility), the maximum stress reached (strength), and the energy density of mechanical deformation until failure (toughness) under extension, all of which are important for determining the workable range of strains and stresses over which the system maintains its integrity. Addressing these questions will help guide the rational design of biomimetic soft materials with tunable mechanics and provide insights into the rigidity and fracture-resistance of load-bearing such as cartilage [89, 95].

The cytoskeleton is a composite scaffold made of networks of different types of biopolymers, primarily actin filaments and microtubules, and motor proteins. Its mechanical response depends on the concentrations of these biopolymers. Motivated by this, we study a model that combines two structure-function frameworks: a double network (DN) made of a network of stiff filaments (microtubules) interacting with a network of flexible filaments (actin), and rigidity percolation theory. The contractility produced by motor proteins are also incorporated in the model. In chapter 3, we presented the results of our simulations of the actin-microtubule network with motor proteins. Specifically, we focused on how the mechanical response of the network changes with varying concentrations of the biopolymers and motor proteins. We also examined the role of the motor proteins in regulating the contractility of the network.

This work in chapter 4 builds on previous works [42, 55] of quasi-species dynamics models that elucidate the life cycle of viruses, and that emphasize the need for the study of therapeutics and their effects on the virus population. These works show the existence of a phase shift between different viral strategies. In light of the current Covid-19 pandemic, interest in the genetic variability of the virus and its role in developing antivirals and vaccines has been rising. Here, we present our study of the role of therapeutics in three critical phases of the viral life cycle: infection, reproduction process, and fecundity. We found an interesting linear relation of the viral load as a function of fecundity and a power law with the reproductive rate of the virus. In contrast, the number of viruses in the cell changes in an unexpected way with a change in the infection rate of the virus. Using this simplified model of the virus and its evolution and mutation, we highlight the possible effectiveness of therapeutics based on the part of the life cycle being influenced.

We have three chapters [Chapter 2,3,4] for the studies of 1) Mechanics and fracture properties of double networks in tissues such as cartilage, 2) Mechanics and contractility of double networks in cytoskeletal networks such actin-microtubule network driven by motor proteins, and 3) The response of a virus population to anti-viral therapeutics that target various stages of the viral life cycle.

Chapter 2

Mechanics of Biopolymer Network in Tissues

2.1 Double Network System in Cartilage

This chapter is about the microscopic modeling of articular cartilage with the aim of understanding it in terms of healthy and diseased tissues. The load-bearing capability of musculoskeletal tissues such as articular cartilage mainly arises from a network-like extracellular matrix made of collagen fibers and proteoglycans [29, 48, 62, 67]. Articular cartilage tissue undergoes several million loading cycles over our lifetimes, and healthy cartilage tissue can bear upto ten times our body weight without fracturing despite limited regenerative capacity. Its remarkable mechanical properties are yet to me matched by synthetic materials, and its difficult to replace it.

However, in the case of cartilage damage due to traumatic injury or diseases such osteoarthritis, the extracellular collagen and aggrecan networks inside the tissue can be degraded due to mechanical stresses or biochemical processes. Especially near the surface where the collagen network is sparse, a small change in the cartilage composition can alter its mechanical properties in a considerable manner which can lead to a reduced modulus and eventually to the tissue failure.

Here, we study the mechanical properties of articular cartilage by combining two structure-function frameworks, (i) a DN made of two interacting disordered networks with very distinct fiber mechanics and (ii) rigidity percolation theory to construct a Rigidly Percolating Double Network model. First, we explain rigidity percolation theory and our rigidly percoalting double network (RPDN). Second, we explain the results in terms of moduli and stresses, followed by the discussion on the varying two parameters - the ratios of the two stretching stiffness constants, and the bond occupation probability of the stiff network.

2.2 Rigidity Percolation Theory

Rigidity percolation theory models a biopolymer network as a disordered network of fibers consisting of flexible, sparsely connected regions and stiff, densely connected regions [6, 17, 19, 25, 84]. When the network is dilute and consists primarily of sparsely connected regions, it does not offer any resistance to shear deformations and has zero shear modulus. In contrast, when densely connected regions span the network, the network has a finite shear modulus. As we tune the density of the fibers in the network from low to high, we cross a threshold in its ability to resist mechanical deformations. In essence, the theory describes the mechanical transition from non-rigid to rigid as a function of the probability of bond presence. This mechanical phase transition is called a rigidity percolation transition and the probability of bond occupation at which it occurs is known as the rigidity percolation threshold.

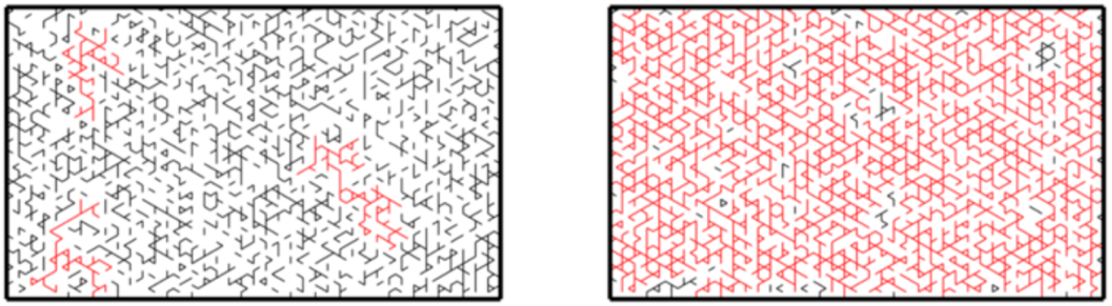

Figure 2.1: The network plot to show the rigidity percolation theory and this kagome lattice figure is published in Biophysical Journal [84].

The rigidly percolating double network model is made of a stiff primary network interacting with a flexible secondary network (Fig. 2.2(a)). In the stiff network, it costs energy to both stretch and bend fibers, while for the flexible network it only costs energy to stretch fibers. We study the shear response and crack propagation in this DN and show that the interplay of the mechanically distinct networks facilitates tunable mechanics and enhanced fracture resistance of the DN. Each of the two networks in the DN is modeled as a disordered kagome network and is constructed following the protocol described in Simulation Details. The bonds in the two net-

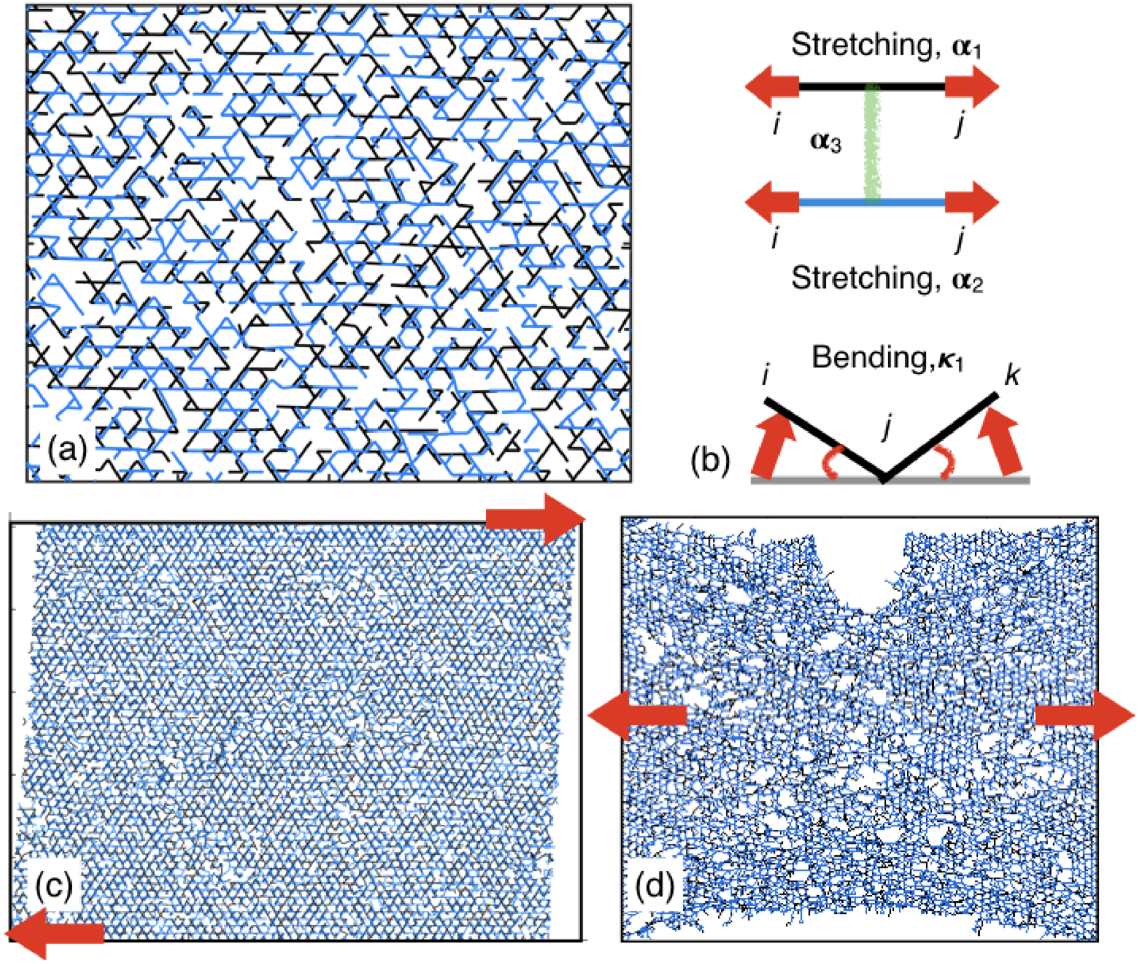

Figure 2.2: Panel (a) represents a schematic of a zoomed-in portion of the DN, and (b) the different contributions to its deformation energy. The black and blue fibers belong to the the stiff and flexible networks respectively. Panels (c) and (d) show representative DNs (with $p_1 = 0.62, p_2 = 0.6$) for our studies of shear response and crack propagation respectively.

works are randomly removed according to two different probabilities, $1 - p_1$ for the stiff network, and $1 - p_2$ for the flexible network, where $0 < p_1, p_2 < 1$ are the bond occupation probabilities. A series of collinear bonds connected end to end constitute a fiber in each network. The stretching modulus of the fibers in the stiff and flexible networks are α_1 and α_2, respectively, where $\alpha_1 > \alpha_2$, and the bending modulus of the fibers in the stiff network is κ_1. The two networks interact with each other via Hookean springs with spring constant α_3 between the midpoints of the corresponding bonds in the networks; for this interaction to be non-zero the corresponding bonds must be present in both networks. See Figure 2.2 (b) for illustration of the properties of the bonds in the networks. Unless otherwise noted, we have used the following biologically relevant parameters in the results presented: $\alpha_2/\alpha_1 = 0.1$, $\kappa/\alpha_1 = .004$ [84], and $\alpha_3 = \alpha_1 + \alpha_2$ chosen to be the effective spring constant of two springs α_1 and α_2 in parallel. Simulations for smaller values of α_3 yielded qualitatively similar results and the percolation thresholds were unchanged. The details of changing parameters are included in Discussion session the chapter.

2.3 Model of Rigidly Percolating Double Network (RPDN)

The rigidly percolating double network model is made of two disordered networks, a stiff network and a flexible network, interacting with each other. Each network is constructed by following the protocol described in [84] where we lay down infinitely long fibers in two dimensions in a Kagome lattice-based network, i.e. we start with a fully ordered lattice. To create a broad distribution of filament lengths, bonds are removed uniformly and in an uncorrelated manner from each network with a given probability: $0 < p_1 < 1$ for the stiff network and $0 < p_2 < 1$ for the flexible network. The bond occupation probabilities p_1 and p_2 can be tuned independently of each other. Within each network, when two fibers cross, we assume a crosslink such that the two crossing fibers can rotate freely but cannot slide relative to each other. Stretching energy of a network is calculated by computing the energy cost stretching or compression of individual bonds and then summing over all the bonds present in the network. Bending energy of a network is calculated by computing the energy of bending of pairs of bonds sharing a node which make a 180 degree angle in the initially undeformed network, and then summing over contributions from all such pairs of bonds present.

The total energy cost of deforming this double network is given by:

$$\begin{aligned}
E_1 &= \frac{\alpha_1}{2} \sum_{<ij>} p_{1,ij} (\mathbf{r}_{ij} - \mathbf{r}_{ij0})^2 \\
&+ \frac{\kappa_1}{2} \sum_{<\widehat{ijk}=\pi>} p_{1,ij}\, p_{1,jk} \;\; \Delta\theta_{ijk}^2 \\
E_2 &= \frac{\alpha_2}{2} \sum_{<ij>} p_{2,ij} (\mathbf{s}_{ij} - \mathbf{s}_{ij0})^2 \\
E_3 &= \frac{\alpha_3}{2} \sum p_{1,ij}\, p_{2,ij} (\mathbf{x}_1 - \mathbf{x}_2)^2,
\end{aligned} \tag{2.1}$$

where E_1 is the deformation energy of the stiff network, E_2 is the deformation energy of the flexible network, and E_3 is the deformation energy of the bonds connecting the two networks which are modeled as Hookean springs as mentioned earlier. In E_1, the first term corresponds to the energy cost of fiber stretching, and the second term to fiber bending [84]. In E_2, we have a similar contribution for fiber stretching, but there is no energy cost of fiber bending. The indices i, j, k refer to sites (nodes) in each lattice based network, such that p_{ij} is 1 when a bond between those lattice sites is present, 0 if a bond is not present. The quantities $\mathbf{r}_{ij}$ and $\mathbf{s}_{ij}$ refer to the vector lengths between lattice sites i and j for the deformed stiff and flexible networks respectively, while $\mathbf{r}_{ij0}$ and $\mathbf{s}_{ij0}$ are the corresponding quantities for the initial undeformed networks. The angles $\Delta\theta_{ijk}$ correspond to the change in the angles between initially collinear bond pairs ij and jk for the deformed and undeformed network respectively.

2.4 Simulation Details

Each network in our double network model consists of 10619 nodes and 21000 bonds when all bonds are present, not counting the connections between the two networks. The system size was chosen to be large enough so that the normalized shear modulus G/G_0 (where G_0 is the network shear modulus when the bond occupation probabilities are both 1) changed minimally with system size, but at the same time not so large that simulations become computationally prohibitive for very floppy networks. The rest length of bonds in each network is 1, i.e. this length scale is used to nondimensionalize all lengths in the system. Similarly, all rigidities are expressed relative to the stretching modulus α_1. In our simulations, we assume a scaled bending to stretching elasticity ratio $\kappa/\alpha_1 = 0.004$ for the fibers in the stiff network [84]. We assume the ratio of the stretching elasticity of fibers in the flexible network to that of the stiff network to be $\alpha_2/\alpha_1 = 0.1$. The scaled interaction strength between the two networks α_3/α_1 is varied across the range $\sim 0.001 - 1$, We used fixed boundaries at the top and bottom and apply deformations via these boundaries, and free boundaries on the sides. Upon application of the shear or extensional deformations, we obtain the equilibrium state of the deformed networks by minimizing the total deformation energy of the double network. The numerical method we used here is a multi-dimensional conjugate gradient (Polak-Ribiere) method [77]. Data are averaged over five simulations unless otherwise indicated.

For the shear response studies (Fig. 2.2(c)), the protocol is as followed. External deformations are applied along the top and bottom boundaries and free boundary conditions are used for the left and right sides of the network. Our simulations of the single network follow the same process, except the deformation energy consists only of contribution from the stiff primary network, since $p_2 = 0$. To obtain the linear mechanical response, we apply a shear strain of 5% at the boundaries, minimize the deformation energy using a multi-dimensional conjugate gradient minimization (Polak-Ribiere) method [77] and calculate the shear modulus [84].

We show the variation of the rigidity percolation threshold of a single network (SN) and four DNs by plotting the shear modulus versus bond occupation probability of the stiff network p_1 (Fig 2.3). The shear moduli G are normalized by their respective values G_0 for fully occupied networks. The four DNs correspond to the four different values of the bond occupation probability $p_2 = 0.2, 0.4, 0.6, 0.8$ of the flexible network. We find that the SN has a percolation threshold $p_{1,c} \sim 0.6$ in agreement with previous results [59], while the DNs have a lower $p_{1,c}$, which decreases with increasing p_2, reaching $p_{1,c} \sim 0.35$ at $p_2 = 0.8$. This is a noteworthy result. On its own, a single stiff Kagome-lattice based fiber network, whose deformation energy consists of stretching and bending energies, has a percolation threshold ~ 0.6 [59], and a single flexible network with only stretching deformation energy and based on such a lattice has a percolation threshold ~ 1. However, when they form a double network, the resulting additional constraints due to their interaction lead to a lower, tunable percolation threshold. These constraints also allow the normalized shear rigidity of the DNs to be larger than that of the SN at the same value of p_1, and this rigidity can be tuned by varying p_2. This result illustrates a mechanism for how the onset of rigidity for biological and synthetic double networks can be drastically modulated through very small changes in filament concentration in the secondary network.

For the crack propagation studies (Fig. 2.2(d)), we create a notch 20 times the bond rest length ($\sim 1/5$ times the system length) at the center of the top boundary following the protocol in Ref.[86], and study how the size of the notch increases as we apply larger and larger tensile strains along the left and right boundaries of the network.

The strains are applied quasi-statically in small increments of 1% up to 70%, and after each application, the total energy is minimized to generate the new equilibrium configuration of the deformed DN. We have made the following assumptions regarding breaking and elastic buckling of fibers: When a bond is stretched above a certain threshold, it will break, and when it is compressed above a certain threshold, it will buckle. Bonds in the stiff network break at 120% of their rest length and buckle at 95% of their rest length. Bonds in the flexible network break at 200% of their rest length, but do not buckle. Broken or buckled bonds will no longer contribute to the deformation energy or rigidity of the network. Fiber breaking is an irreversible process, but buckled fibers in our model can “unbuckle“ when the extra compression is removed.

2.5 Calculation

2.5.1 Modulus and Stress

To demonstrate how the fracture mechanics changes with the stiff network's proximity to its rigidity percolation threshold, we present results for simulations of the DN close to ($p_1 = 0.62$) and away from ($p_1 = 0.80$) the rigidity threshold (Fig. 2.4). The values of p_1 were chosen, so that the DN has a finite rigidity, irrespective of p_2. We also found, for example, that when p_1 was set to 0.55, the DN had zero shear rigidity and exhibited no stresses when p_2 was 0, 0.2, or 0.4. We find that both the Young's modulus (Fig. 2.4(a) and (b)) as well as the stress (Fig. 2.4(c) and

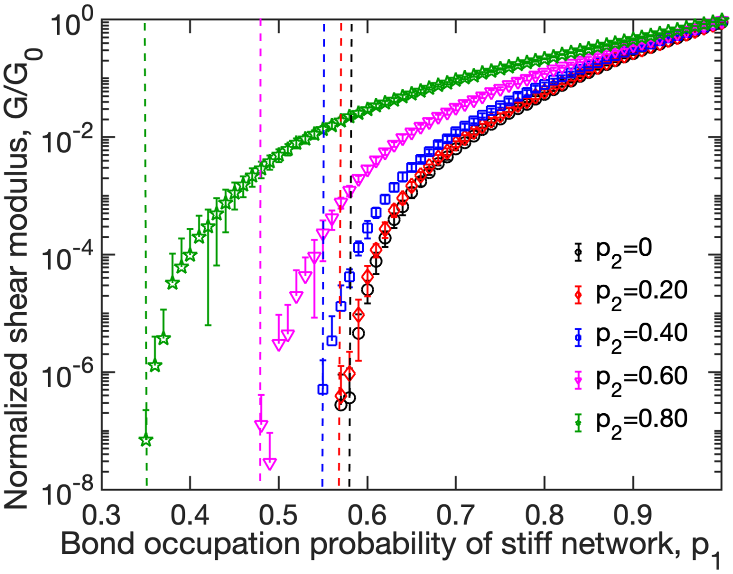

Figure 2.3: The normalized shear modulus (G/G_0) shown as a function of p_1 for an SN (black circles) and four DNs (remaining data). The values of p_2 are shown in the legend. The dashed lines provide guide to the eye for the rigidity percolation transitions. The data is averaged over five runs and the standard deviations are indicated by errorbars.

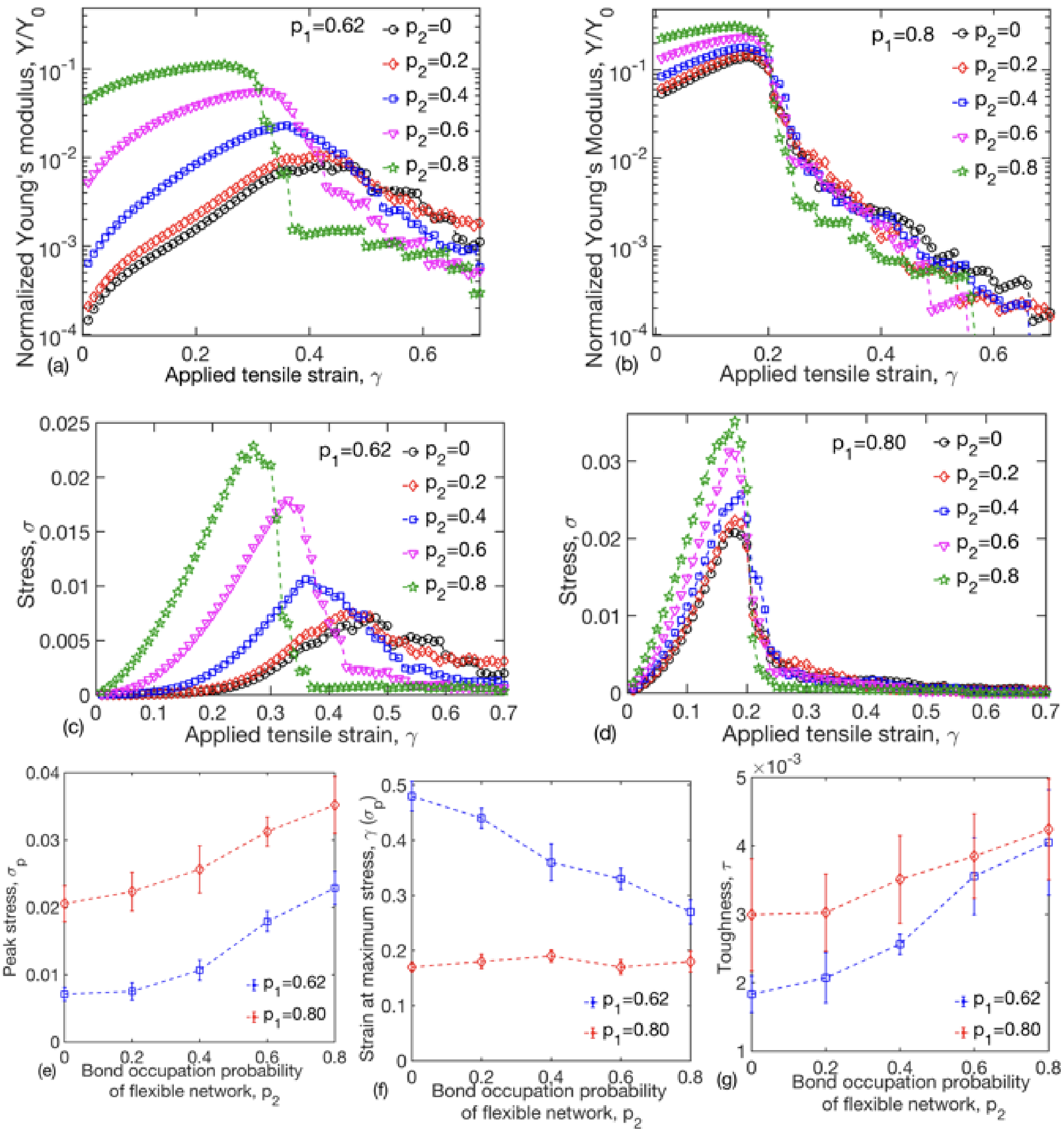

Figure 2.4: Figures (a-b) show the normalized Young's modulus Y/Y_0 and (c-d) show the stresses σ developed in the SN (black circles) and DN (remaining data) as a function of the uniaxial tensile strain γ applied at the boundaries. Figure (a) and (c) corresponds to $p_1 = 0.62$, and figure (b) and (d) to $p_1 = 0.80$; p_2 is as shown in the legend in these figures. Figures (e), (f), and (g) show the peak stress (σ_p), and the strain at peak stress ($\gamma(\sigma_p)$), and the toughness (τ) as a function for p_2 for the data shown in (c) and (d). The stress is expressed in units of $\alpha_1 \times \rho$, where ρ is network concentration in total fiber length per volume for the stiff network, and the toughness, which is the total area under the stress-strain curves shown in (c) and (d), has the same unit. The data is averaged over five runs and the standard deviations are indicated by errorbars.

(d)) developed in the network initially increase with strain and reach a maximum as previously floppy regions become stretched and align to resist deformation. Once the fibers in the network start to experience strains larger than their stretching (or elastic buckling) thresholds, however, they break (or buckle), causing the network to soften. Remarkably, we find that when the stiff network is close to its rigidity threshold, the normalized Young's modulus, the maximum or peak stress, and the strain at maximum stress (onset of failure), can be shifted dramatically by the flexible network. This tunability arises because the sparsely populated stiff network allows the DN to undergo non-affine rearrangements [17, 36, 39], leading to large variations in rigidity. The mechanics can be further varied using the coupling between the two networks in the DN. This is explained in the discussion session.

We quantify these trends by comparing the peak stress σ_p, strain at maximum stress $\gamma(\sigma = \sigma_p)$, and the fracture toughness τ versus p_2 for both DNs in Fig 2.4. Here we have used the total area under the stress-strain curve as a measure of the network's fracture toughness. We find that the peak stress increases with p_2 for both DNs due to the additional constraints introduced by the secondary, flexible network. The strain at maximum stress decreases with p_2 when the stiff network is close to the percolation threshold and remains nearly constant when the stiff network is far from the percolation threshold. Thus, the additional constraints introduced by the secondary network play a much greater role in restricting deformation when the stiff network is near the rigidity percolation threshold. Finally, we find that while the network toughness increases for both cases, the increase is greater for the network near the rigidity percolation threshold. This result is somewhat surprising. The measure of toughness used here is typically proportional to the product of the peak stress and strain at the onset of failure where the material fails abruptly. Here, while this product remains nearly constant for the $p_1 = 0.62$ data as p_2 in varied, the measured area under the stress-strain curve increases with p_2. This is because as the network fails gradually, the decrease in stress is far less abrupt than in typical materials, and the network toughness is substantially increased.

2.6 Results

These results highlight an important and novel mechanism in shear and fracture mechanics of DN polymer systems: a secondary flexible network can be used to dramatically tune the mechanics of a composite DN when the primary stiff network is just above the rigidity percolation threshold. In this regime, decreasing p_2 allows internal stresses to relax through non-affine deformations and enables the DN to remain intact until larger strains, while increasing p_2 leads to larger mechanical reinforcement from the secondary network. The results show how the DN can be modulated to either be extensible, breaking gradually, as is the case for low p_2 or be stronger, breaking in a more brittle fashion, as is the case for high p_2. In contrast, far above the rigidity threshold, the primary stiff network is far too dense and rigid to allow any non-affine network restructuring or rearrangement of the DN by varying the density of the secondary flexible network; the DN is brittle, and breaks before stresses can be dissipated. The low p_2 limit is particularly important in biological tissues such as articular cartilage when it is undergoing osteoarthritis, where the proximity of the stiff (collagen) network to the rigidity percolation threshold varies as a function of tissue depth and the reinforcing flexible network is increasingly removed as the disease progresses [32, 84, 101].

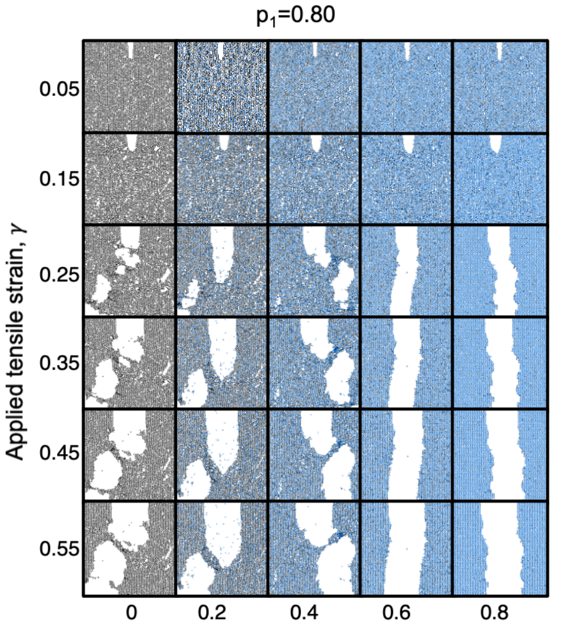

(a) Bond occupation probability of flexible network, p_2

To illustrate the above-mentioned mechanism visually, we present stills from simulations of crack propagation in DNs with $p_1 = 0.62$ and 0.80 as a function of the applied tensile strain γ and p_2 (Fig. 2.5). We find that when the stiff network is far above the rigidity threshold ($p_1 = 0.80$, Fig. 2.5(a)), the DN ruptures abruptly at $\gamma \sim 0.2$ for all p_2 values, though the crack morphology is more uniform at higher p_2. In contrast, when the stiff network is close to the rigidity threshold ($p_1 = 0.62$,

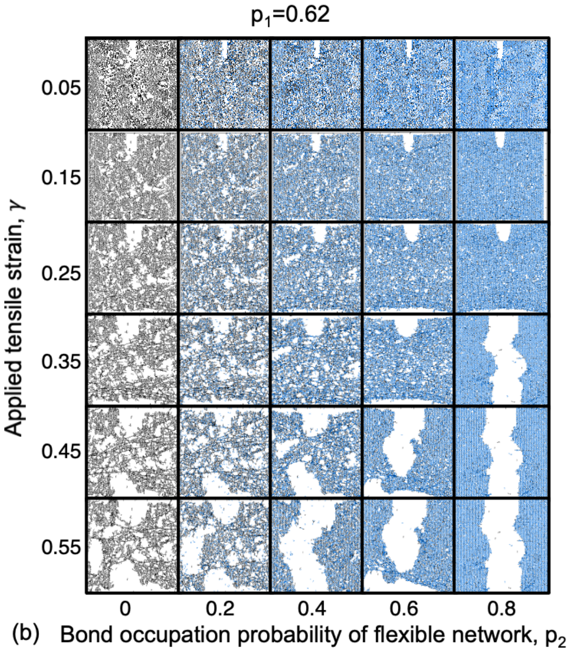

Figure 2.5: Deformation and fracture of the SN ($p_2 = 0$) and the DN ($p_2 \neq 0$) as a function of increasing p_2 (x-axis) and applied strain (y-axis). The value of p_1 is set to 0.80 in (a) and to 0.62 in (b), i.e. the stiff network is just above the rigidity percolation threshold in (a) and far above this threshold in (b). Both the SN and DN were subjected to uniaxial strains applied at the boundary and the strain was increased in steps of 1%.

Fig. 2.5(b)), we observed a wider range of responses. For $p_2 = 0$, 0.2, and 0.4 the networks are extensible, initially developing microcracks that are distributed throughout. With increasing strain, these microcracks grow and the network decreases its rigidity while maintaining a percolated structure. For $p_2 = 0.6$ and 0.8 the networks are more brittle, rupturing less homogeneously and maintaining their rigidity up until the point of failure.

2.7 Discussion

2.7.1 Varying the inter-network interaction of the two networks

Previously, we set the elastic interaction between the two networks $\alpha_3/\alpha_1 = 1.1$, with the assumption that one could think of α_3 as an effective spring. Here we relax this assumption and discuss results for $\alpha_3/\alpha_1 \sim$ 0.001-1. We find that varying α_3/α_1 does not affect the main conclusion of our paper namely that: the secondary flexible network modulates the mechanics of the composite DN far more effectively when the primary stiff network is near its rigidity threshold. However, α_3/α_1 can be used to tune the micromechanics of the network.

In Figures 2.6 and 2.7 we present data for $\alpha_3/\alpha_1 = 0.01$. These figures show that normalized Young's modulus and strain at maximum stress show significant variation with p_2, when p_1 is 0.62 but not when it is 0.80, as shown before. In addition, the rigidity percolation threshold on the DN remains the same. In Figure 2.8 , we present the variation of the normalized shear modulus with p_1 for different values of p_2 for two cases; when $\alpha_3/\alpha_1 = 0.01$ and when it is 0.001. The rigidity percolation thresholds for a given p_2 does not depend on α_3/α_1. This is expected because the percolation threshold is set by the balance between the degrees of freedom and constraints in the system. Finally, varying the coupling between the networks does impact the values of the Young's modulus, the maximum stress, and the strain at maximum stress as seen in Fig. 2.9 . A weaker coupling (smaller α_3) allows for more non-affine deformations of the DN and thus leads to a decrease in its Young's modulus (rigidity), maximum stress (strength) and an increase in the strain at maximum stress (extensibility). These results show that in addition to the axial rigidities of the filaments in the two networks α_1 and α_2, the coupling strength α_3 can modulate deformations and relaxation of the network. Note, however, that the bonds corresponding to α_3 are present only if the corresponding bonds in the two networks, are both present, i.e., there is no independent source of disorder in the coupling between the networks. Therefore, changing α_3 can only change the shape of the modulus versus bond occupation probability curves and not the rigidity percolation threshold of the composite network for small deformations of the DN when there is no breaking or buckling of bonds.

2.7.2 Varying the ratio of filament stretching stiffness of the two networks

For large deformations that result in breaking and buckling of bonds, we found that changing α_2/α_1 will change the shape of the modulus versus strain and stress versus strain curves, and consequently, the values of maximum or peak stress, and the strain at maximum stress, but the qualitative trends remain unchanged. To illustrate this, in Fig.2.10, we show results from simulations where we set the above-mentioned ratio to 0.2 instead of 0.1. Further, we ran these simulations for $p_1 = 0.7$ in addition to for $p_1 = 0.62$ and $p_1 = 0.8$. In Fig.2.10, panels (a), (b), and (c) show the modulus as a function of applied strain, and panels (d), (e), and (f) show the stress as a function

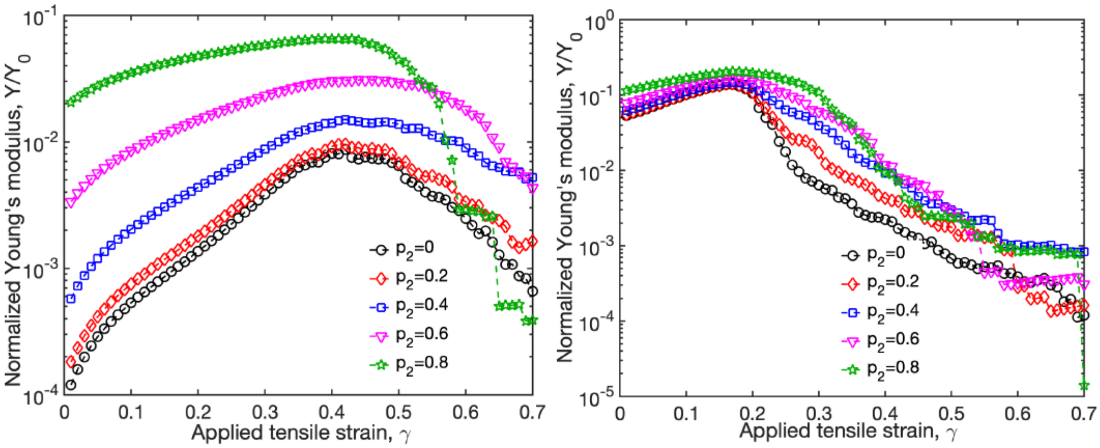

Figure 2.6: The normalized Young's modulus (Y/Y_0) shown as a function of the applied tensile strain, γ, for the bond occupation probability of the stiff network $p_1 = 0.62$ (left figure) and $p_1 = 0.8$ (right figure). The flexible network has a bond occupation probability, p_2 as shown in the legend. The parameters are $\alpha_2/\alpha_1 = 0.1$, $\kappa/\alpha_1 = 0.004$, and $\alpha_3/\alpha_1 = 0.01$.

of applied strain, where the open symbols correspond to a ratio α_2/α_1 of 0.1 and the closed symbols to 0.2. Note that while changing the value of α_2/α_1 led to small quantitative changes (larger rigidities and load-bearing capability for $\alpha_2/\alpha_1 = 0.2$), it did not change the qualitative trends reported before. To further crosscheck this, we also examine the peak or maximum stress the DN can withstand before it starts to soften and the strain at maximum stress. We show these results in Fig.2.11. As expected, we found that the peak stresses are larger when $\alpha_2/\alpha_1 = 0.2$ than when $\alpha_2/\alpha_1 = 0.1$, but the qualitative trends remain the same. Similarly, the qualitative trends for the strain at maximum stress also remain the same, although there are small quantitative changes.

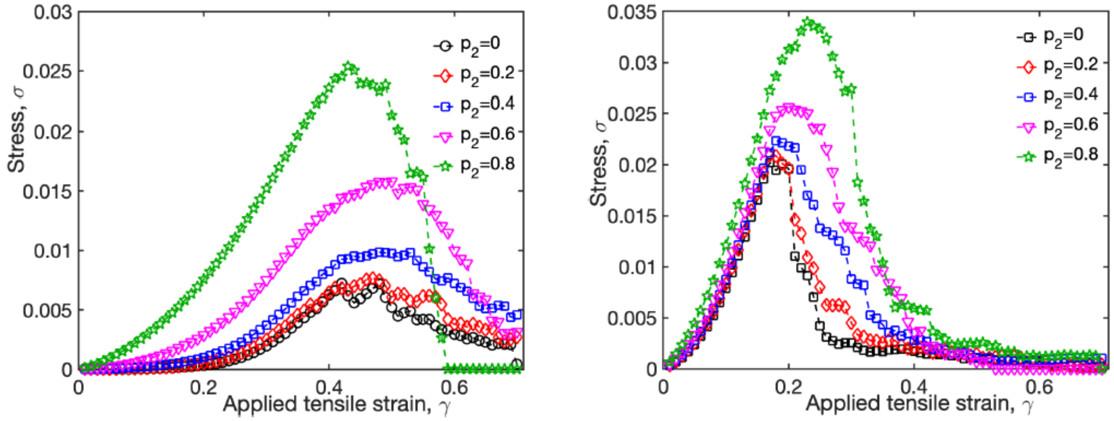

Figure 2.7: The stress σ shown as a function of the applied tensile strain, γ, for the bond occupation probability of the stiff network $p_1 = 0.62$ (left figure) and $p_1 = 0.8$ (right figure). The flexible network has a bond occupation probability, p_2 as shown in the legend. The parameters are $\alpha_2/\alpha_1 = 0.1$, $\kappa/\alpha_1 = 0.004$, and $\alpha_3/\alpha_1 = 0.01$

2.7.3 Varying the bond occupation probability of the stiff network

We first show data for values of p_1 close to the rigidity percolation threshold of the primary network ($p_c \sim 0.58$ in our simulations) with p_2 set to 0. In Fig.2.12 below, we show the data, averaged over five runs, for the normalized shear modulus, G/G_0 as a function of for the two extreme cases: $p_2 = 0$ and $p_2 = 1$. Note that while for both $p_2 = 0$ in Fig.2.12 (a) and $p_2 = 1$ Fig.12 (b), G/G_0 first increases very slowly (when $|p_1 - p_c|$ is 0.001 or less), then more rapidly, the increase spans many more decades for $p_2 = 0$. This is also clearly seen in difference in the logarithms of the normalized shear modulus for $p_2 = 1$ and $p_2 = 0$, shown in Fig.2.12 (c), as a function of $|p_1 - p_c|$. As expected very close to a phase transition, this difference is large when $|p_1 - p_c| = 10^{(-4)}$ (and over 5 orders of magnitude difference in the normalized shear modulus), and then decreases steadily as we move away from p_c; when we reach $|p_1 - p_c| = 10^{(-1)}$ the two normalized moduli difference only by an order of magnitude. These trends are corroborated data for the corresponding data for the peak stress for large deformations leading to fracture shown in Fig.2.13.

Next, we show data for four different values of p_1, 0.62; 0.63; 0.7; 0.8, from near p_c to far away from p_c. We show the variation in dG/dp_2 as a function of p_2 in Fig. 15, the normalized Young's modulus vs. strain in Fig.2.15 (a-d), stress vs strain in Fig.2.16 (a-d), peak stress vs p_2 in Fig.2.17 (a), and strain at maximum stress vs p_2 in Fig.2.17 (b). In all these figures. we observe large variations in the DN's properties for $p_1 = 0.62$ and 0.63, and these variations are attenuated as p_1 is increased, with rather small variations for $p_1 = 0.8$. These results show again that the tunability of network mechanics and fracture properties is most striking when the primary network is near its rigidity percolation threshold.

2.7.4 Understanding Tunability and Crack Propagation

In sum, we find that the rigidity percolation threshold for the stiff network can be varied, even significantly lowered by changing the flexible network's concentration. Second, the flexible network can modulate the mechanics of the DN (strength, extensibility, and toughness) far more efficiently when the stiff network is just above its rigidity percolation threshold. Third, the DN can further be tuned to either be more extensible for low concentrations of the flexible network, breaking gradually, or

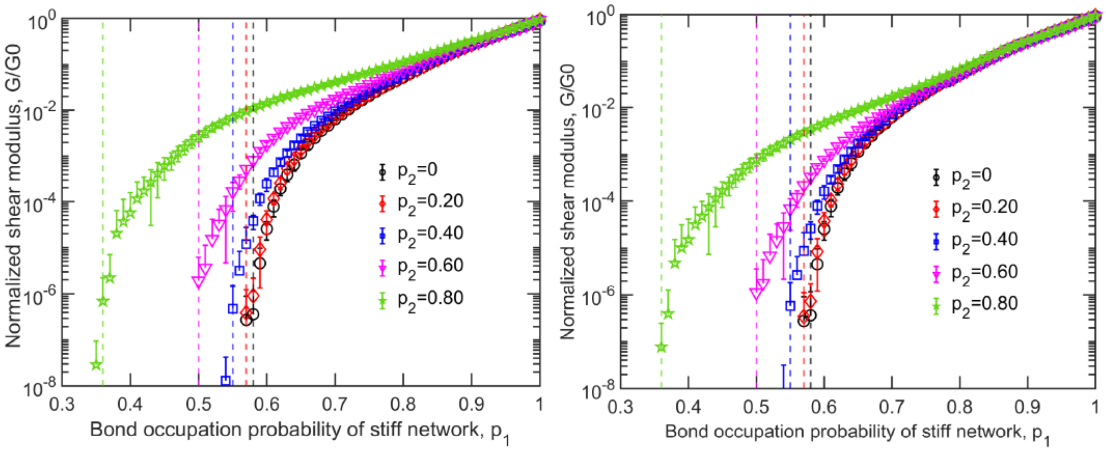

Figure 2.8: The normalized shear modulus (G/G_0) shown as a function of the occupation probability,p_1, of the stiff network for two different α_3/α_1, 0.01 (left figure) and α_3/α_1, 0.001 (right figure). The flexible network has a bond occupation probability, p_2 as shown in the legend. The parameters are $\alpha_2/\alpha_1 = 0.1$, $\kappa/\alpha_1 = 0.004$, and $\alpha_3/\alpha_1 = 0.01$.

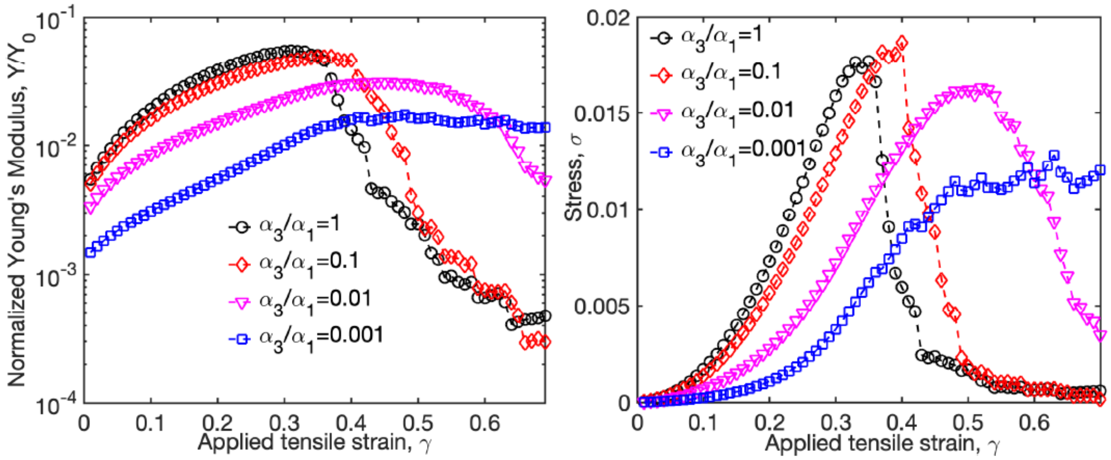

Figure 2.9: The normalized Young's modulus, Y/Y_0, and stress, σ, as functions of the uniaxial tensile strain γ applied at the boundaries. In this figure, $p_1 = 0.62$ and $p_1 = 0.60$, and α_3/α_1 has values as shown in the legend.

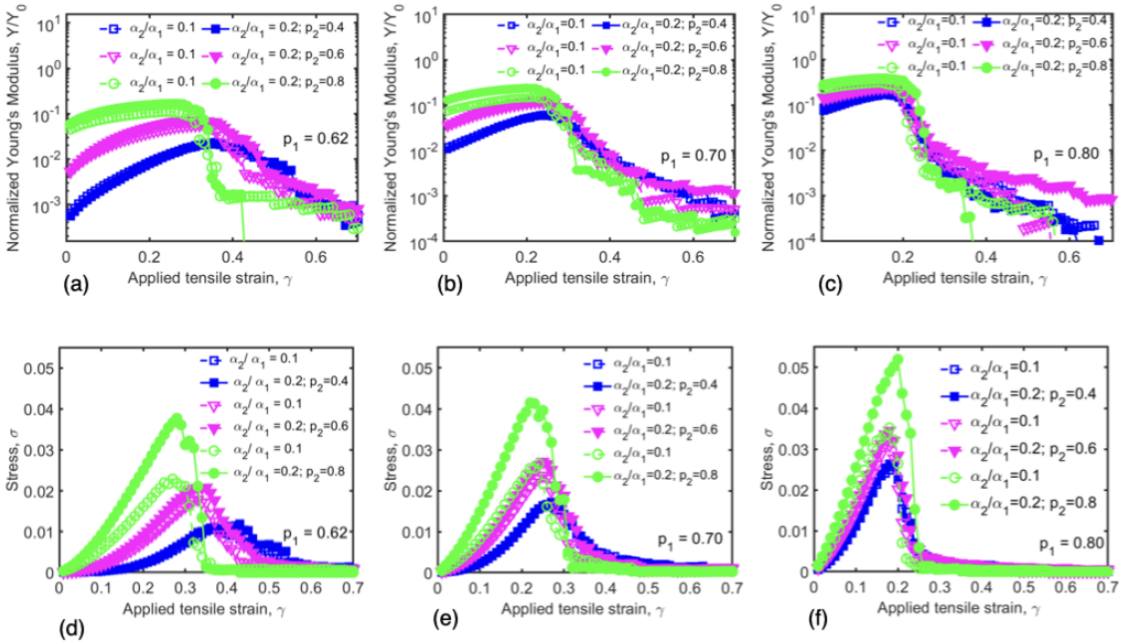

Figure 2.10: The normalized Young's modulus, Y/Y_0, and stress, σ, as functions of the uniaxial tensile strain γ applied at the boundaries, for three different values of p_1. The ratio α_2/α_1 has values as shown in the legend.

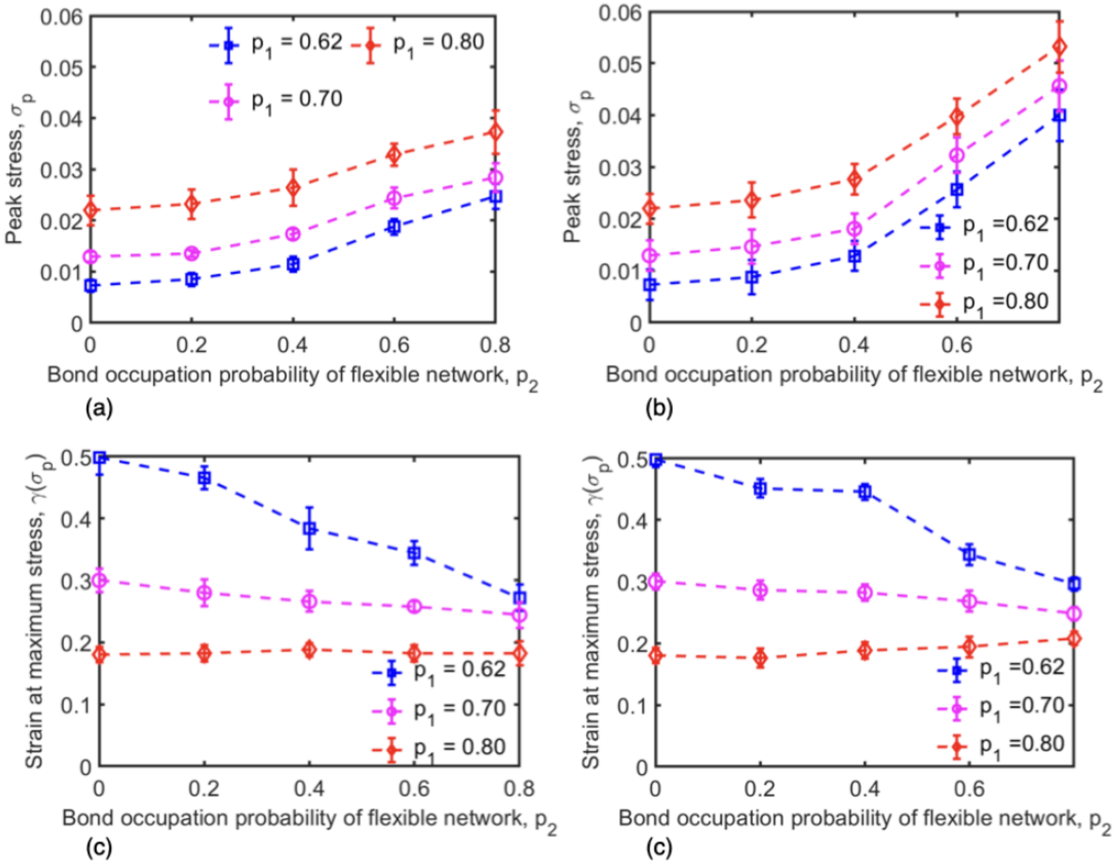

Figure 2.11: The peak stress and strain at maximum stress as functions of bond occupation probability of the flexible network p_2. Panels (a) and (b) show the peak stress when α_2/α_1 - 0.1 and 0.2, respectively, while Figures (c) and (d) show the respective strain at maximum stress. The data represent three values of p_1 shown in the legend.

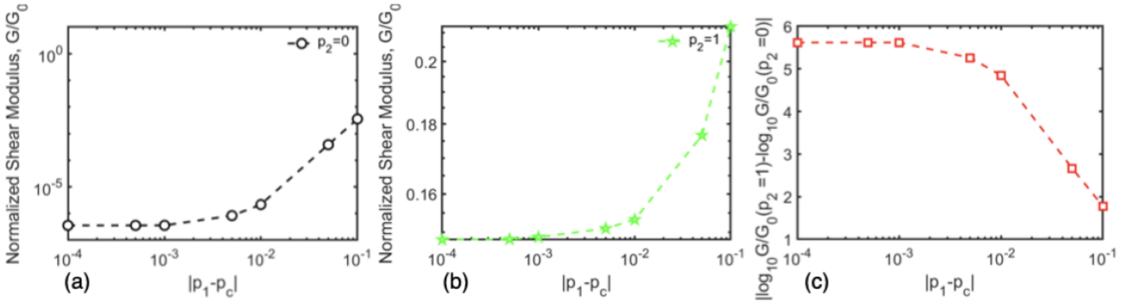

Figure 2.12: Figure shows the normalized shear modulus (G/G_0) as a function of the deviation from the bond occupation probability p_1 from the rigidity percolation threshold p_c(0.58) for $p_2 = 0$, for the two extreme cases of $p_2 = 0$ in (a) and $p_2 = 1$ in (b). In figure (c), we show the difference in the logarithm of the normalized modulus values for the occupation probabilities shown in (a) and (b).

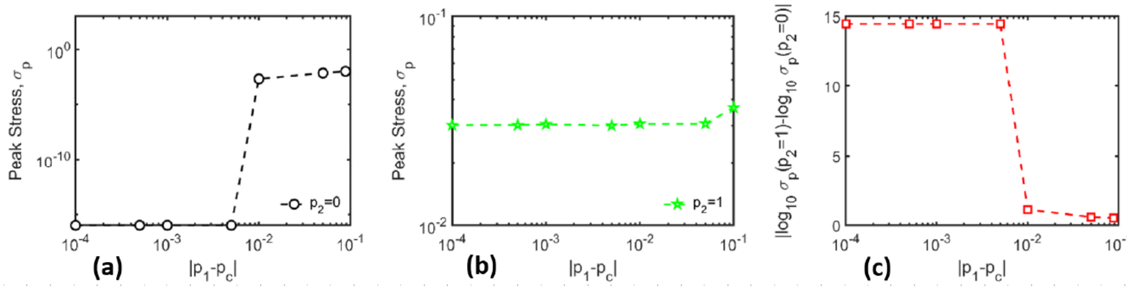

Figure 2.13: Figure shows the peak stress as a function of $|p_1 - p_c|$, where (p_c 0.58) for the two extreme cases of $p_2 = 0$ in (a) and $p_2 = 1$ in (b). In figure (c), we show the difference in the logarithm of the peak stress values for the occupation probabilities shown in (a) and (b).

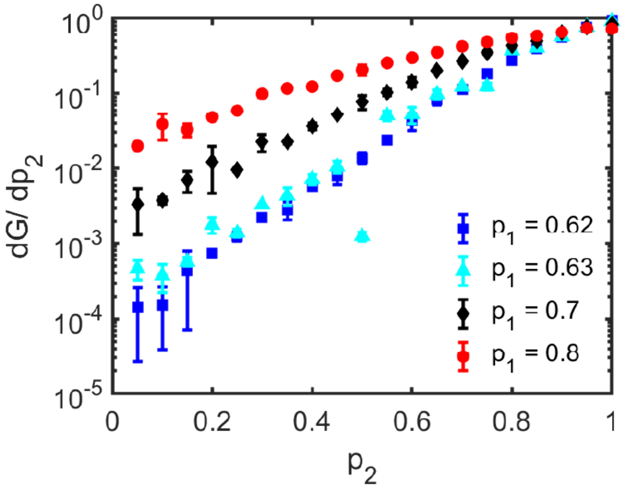

Figure 2.14: Figure shows the derivative of normalized shear modulus G/G_0 as a function of the bond occupation probability p_2, for different values of p_1 (shown in legend).

be stronger, breaking in a more brittle fashion for high concentrations of the flexible network. Our results show how structure and composition can be tuned to resist cracks. Importantly, this ability to tune the failure characteristics could have numerous important applications. For example, our simulations suggest that it may be possible to construct DNs with varying compositions to guide the trajectory or even stall cracks propagating through the material. We speculate, given the similarity of some of the crack morphologies in our simulations (e.g., $p_2 = 0.6, \gamma = 0.35$ in Fig. 2.5b) to the experimentally observed fracture of articular cartilage tissue (see for example Figure 4 in [86]) it is possible that cartilaginous tissues may already be employing such mechanisms. The similar crack propagation is found in some experimental data of articular cartilage [83, 87].

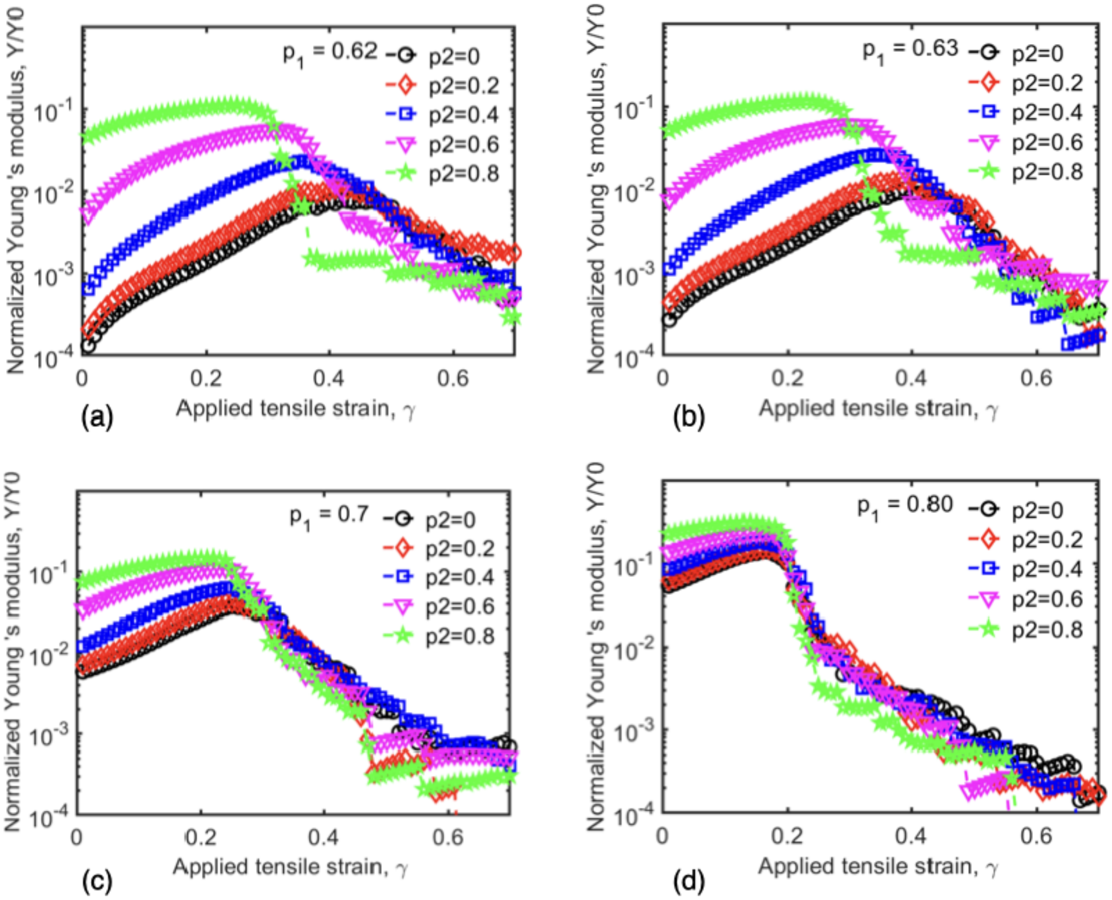

Figure 2.15: Panels (a-d) shows the normalized Young's modulus Y/Y_0 of the SN (black circles) and DN (remaining data) as a function of the uniaxial tensile strain γ which is applied at the top boundaries, with p_1 set to 0.62 (a), 0.63 (b), 0.7 (c), and 0.8 (d).

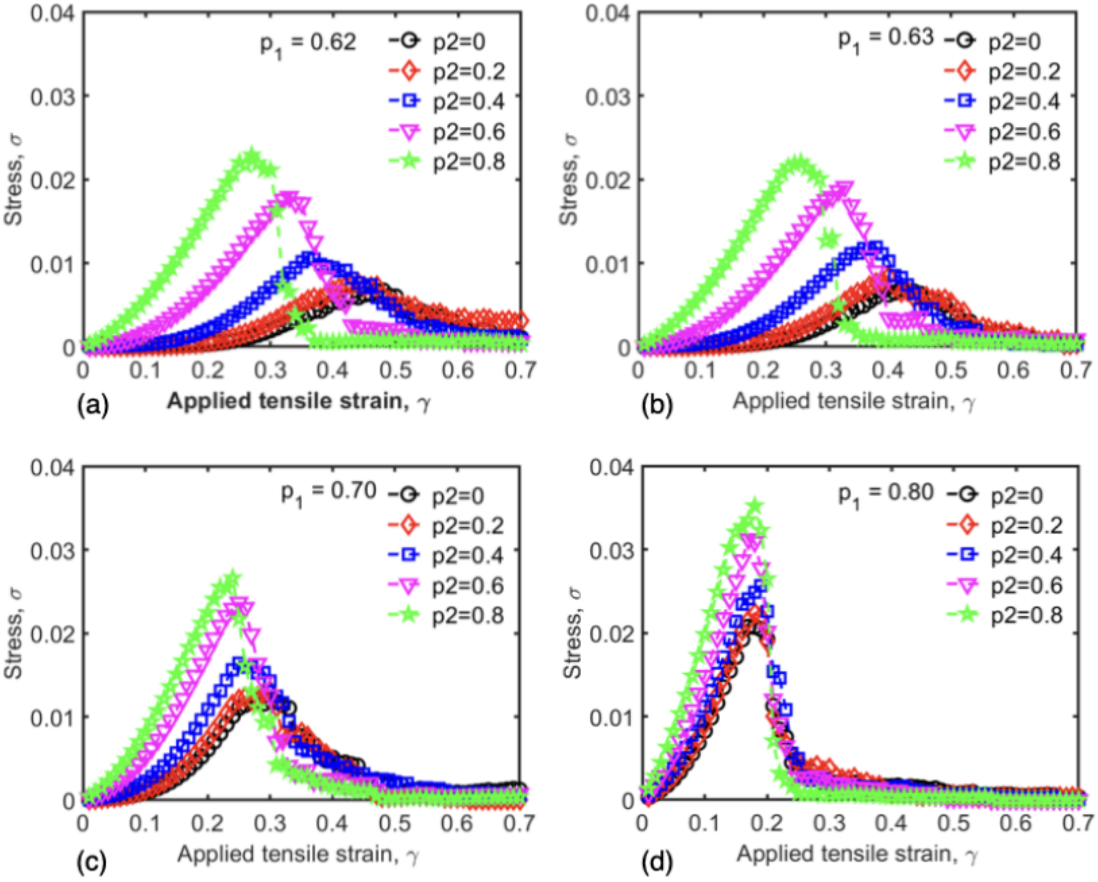

Figure 2.16: Panels (a-d) shows the stress σ developed in the SN (black circles) and DN (remaining data) as a function of the uniaxial tensile strain γ which is applied at the top boundaries, with p_1 set to 0.62 (a), 0.63 (b),0.7 (c), and 0.8 (d).

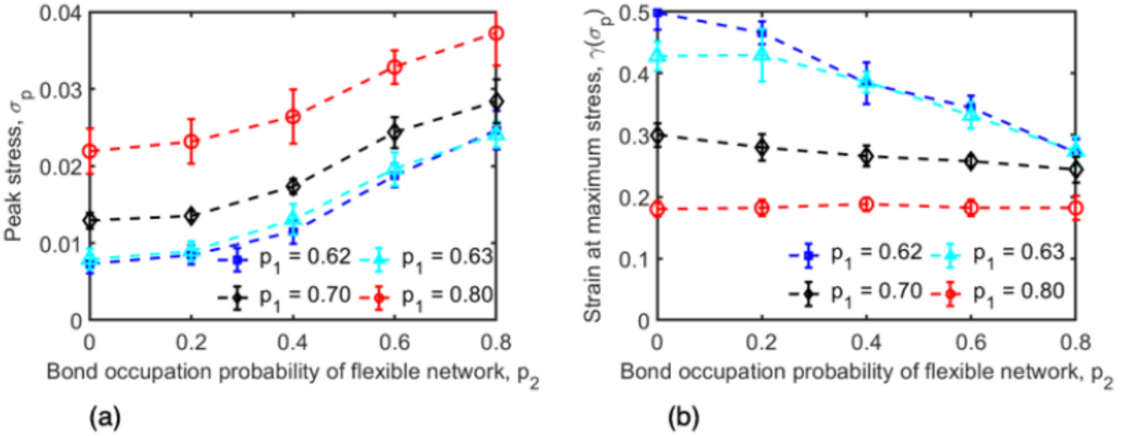

Figure 2.17: Panels (a) and (b) respectively show the maximum or peak stress σ_p and strain at this maximum stress plotted against the bond occupation probability of flexible network p_2

Over the last decade, double network systems have become technologically important because they have enhanced toughness, delayed gel fracture, and controllable peeling behaviors. Our results illustrate a mechanism that allows for controlling how much the secondary network can do to attenuate or relax stresses in the primary network, and can inform the choice of materials and microstructural parameters for the rational design of biomimetic soft composite materials with desired properties. In our case, our result could help in inventing a substitute and synthetic material for a healthy cartilage. In sum, if we would like to achieve the tunable and crack resistant material, the first network should be just above rigidity percolation threshold and the second network should be moderately dense. This choice will allow the double network to bear mechanical stresses but still allow low energy non-affine rearrangements of the network. Note that very sparse stiff (collagen) network would resemble the tissue collapse in the event of the loss of second network (proteoglycan) and the disorganization of collagen during the early osteoarthritis [101].

2.8 Hysteresis Simulations

Biological systems efficiently maximize robustness with tunability and self-healing properties. Here we examine if the Rigidly Percolating Double Network (RPDN) framework that allows for breaking and buckling of bonds under large stresses shows hysteresis, i.e. difference in the strain-strain relationships during loading and unloading. We study this in two samples of double networks– with or without a notch.

The simulations are done similar to the earlier studies described in this chapter. The bending-to-stretching elasticity ratio is $\kappa/\alpha_1 = 0.004$ for all fibers in the stiff network, and the ratio of the stretching elasticity of fibers in the second network to the first network is 0.1. The scaled interaction term is the smallest at 0.001, and we apply the deformation quasi-statically with a step of 1 percent. To simulate the hysteresis loop in the RPDN model, we added an additional step. For each pair of p_1 and p_2, we find the maximum or peak strain and run the simulations up to 10 percent of the maximum strain to simulate the hysteresis loop.

The main idea of simulating the hysteresis loops for our RPDN model is to find out whether the deformation in the double network system is reversible or not. Before going into details of the simulated hysteresis loops, we want to repeat the simulations we did in the previous session. Figs. 2.18 and 2.19 are replications of the previously

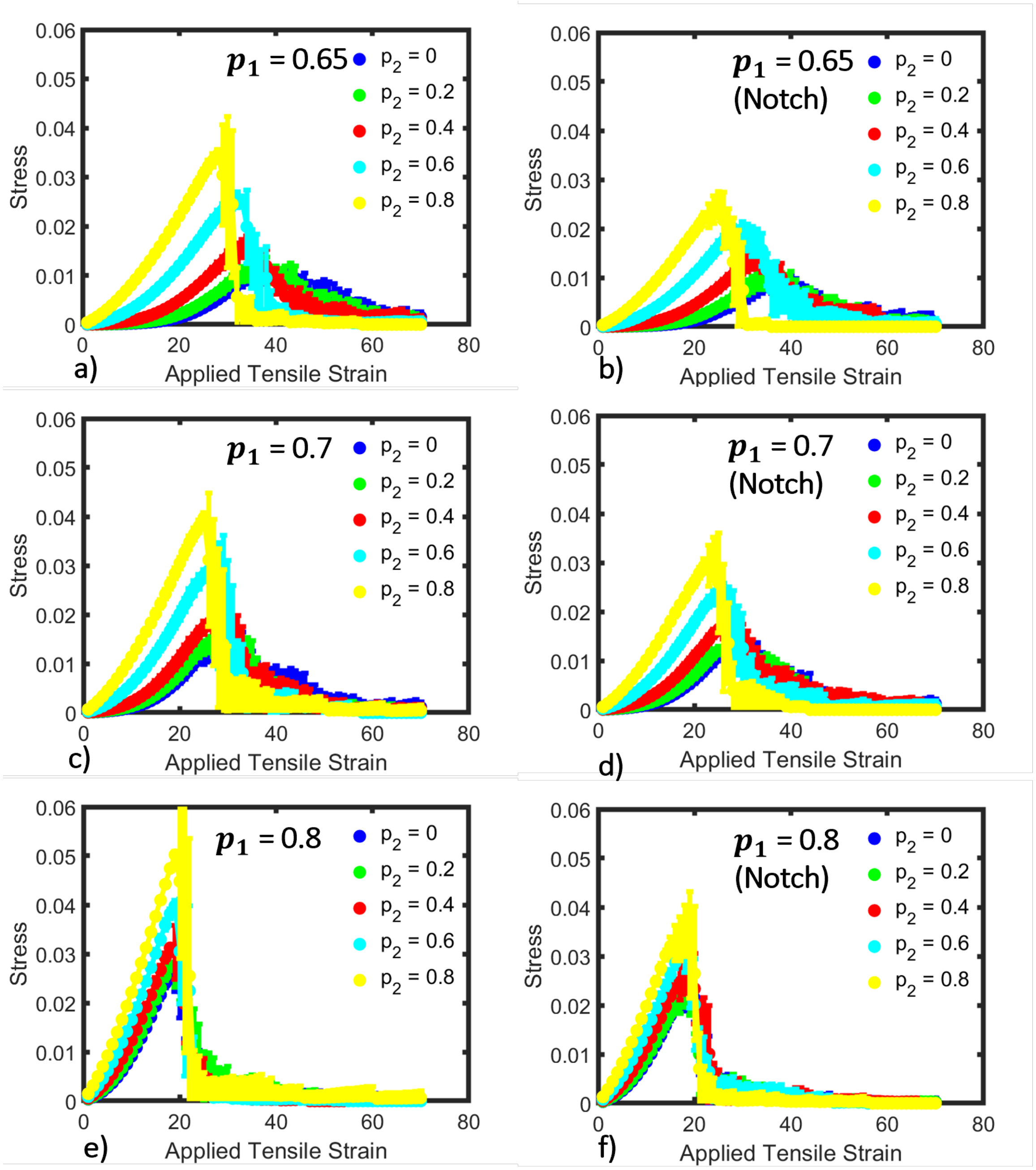

Figure 2.18: Figures show the stresses in the DN system without a notch (first column) and with a notch (second column) as a function of Applied Tensile Strain. Panels (a), (c), and (e) respectively shows the stress vs. strain for $p_1 = 0.65$, 0.7, and 0.8 without a notch. Figures (b), (d) and (e) have similar plots for the system with a notch.

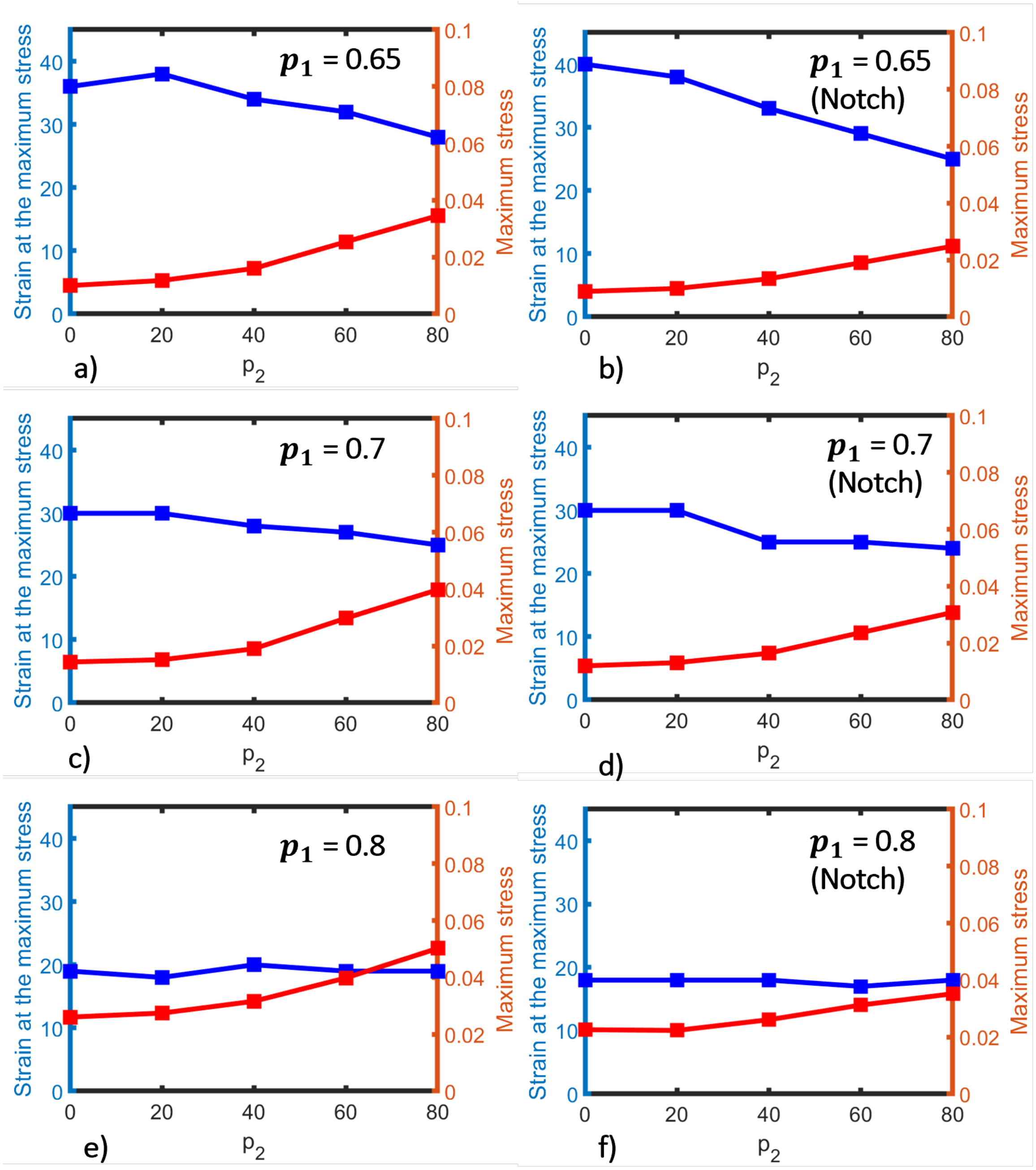

Figure 2.19: **(a)** On the left y-axis using blue color, figures in the DN system without a notch (first column) and with a notch (second column) while on the right y-axis using red color, maximum stress is plotted. Panels (a), (c), and (e) respectively show the strain at the maximum stress as a function of p_2 for $p_1 = 0.65$, 0.7, and 0.8 without a notch. Figures (b), (d) and (f) have similar plots for the system with a notch.

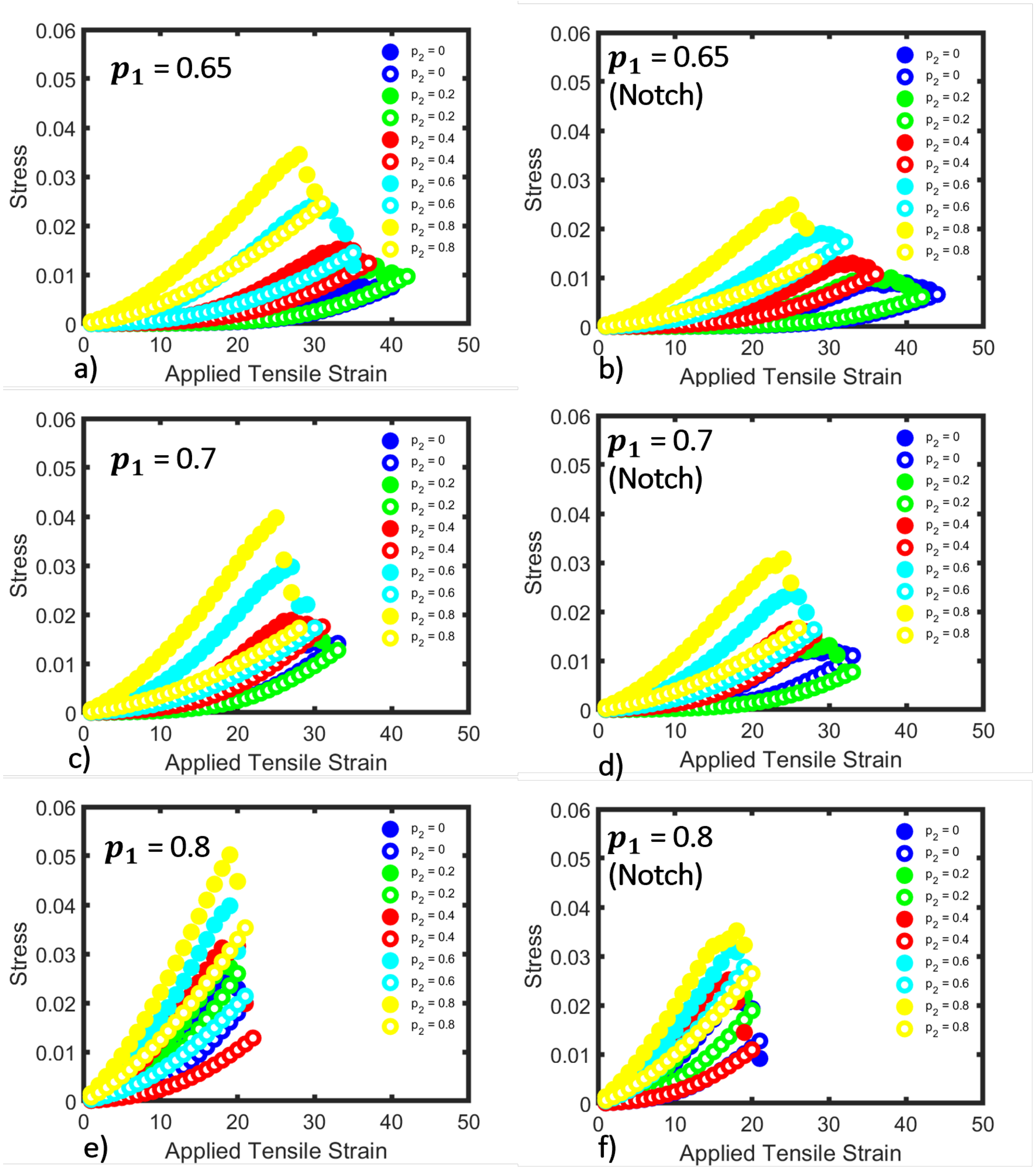

Figure 2.20: Figures show the stresses in the DN system without a notch (first column) and with a notch (second column) as a function of applied tensile strain. Panels (a), (c), and (e) respectively shows the stress vs. strain for $p_1 = 0.65$, 0.7, and 0.8 without a notch. Figures (b), (d) and (f) have similar plots for the system with a notch.

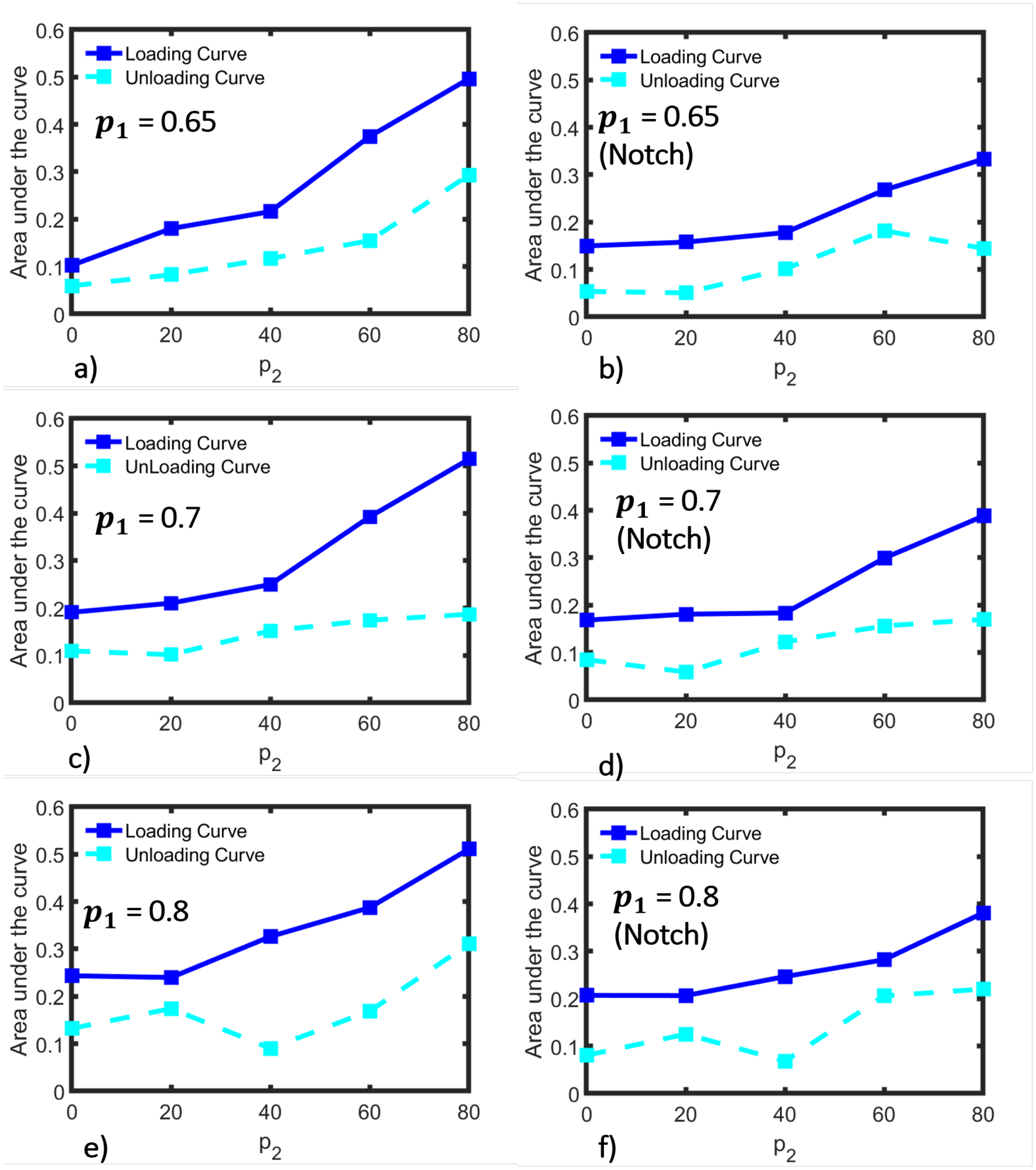

Figure 2.21: Figures show the areas under loading and unloading curves in the DN system without a notch (first column) and with a notch (second column) as a function of p_2. Panels (a), (c), and (e) respectively shows the stress vs. strain for $p_1 = 0.65$, 0.7, and 0.8 without a notch. Figures (b), (d) and (f) have similar plots for the system with a notch.

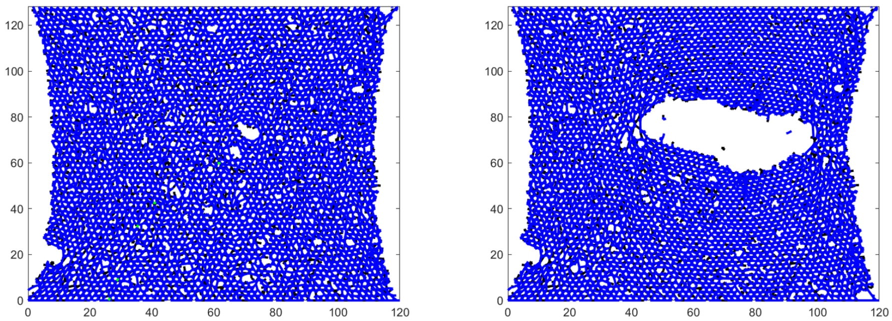

a) p_1 = 0.65, p_2 = 0.8, (loading)

b) p_1 = 0.65, p_2 = 0.8, (unloading)

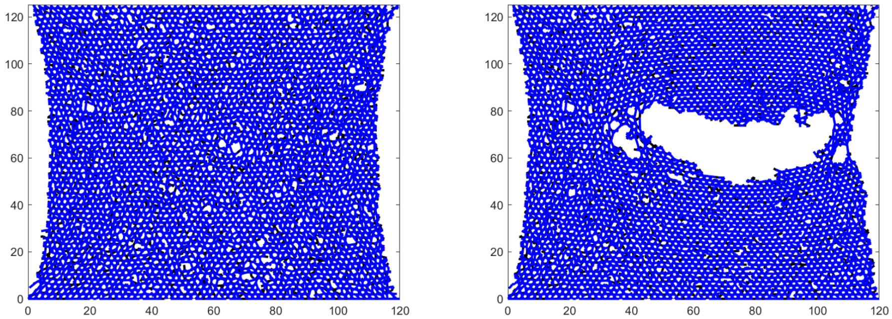

c) p_1 = 0.7, p_2 = 0.8, (loading)

d) p_1 = 0.7, p_2 = 0.8, (unloading)

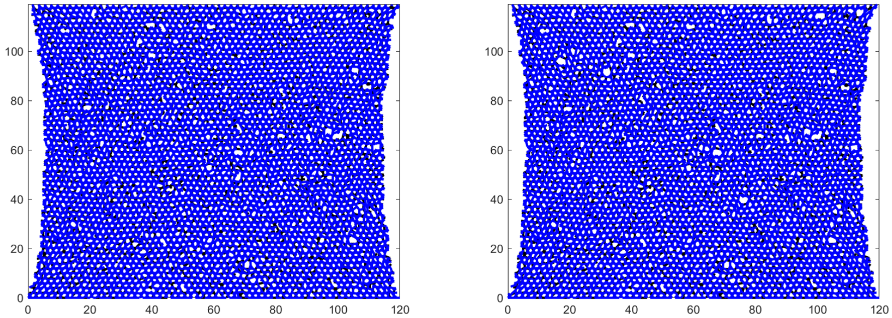

e) p_1 = 0.8, p_2 = 0.8, (loading)

f) p_1 = 0.8, p_2 = 0.8, (unloading)

Figure 2.22: Figures show the network plots of loading curves (first column) and unloading curves (second column) in the DN system **without a notch** at the peak stress. Panels (a), (c), and (e) respectively shows the stress vs. strain for $p_1 = 0.65$, 0.7, and 0.8 without a notch. Figures (b), (d) and (f) have similar plots for the system with a notch.

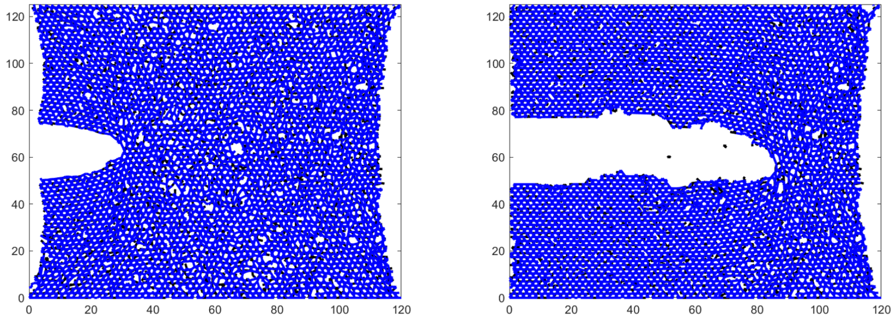

a) p_1 = 0.65, p_2 = 0.8, (loading) b) p_1 = 0.65, p_2 = 0.8, (unloading)

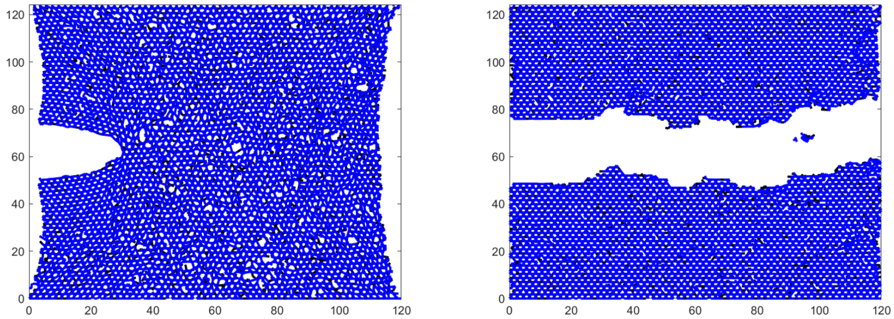

c) p_1 = 0.7, p_2 = 0.8, (loading) d) p_1 = 0.7, p_2 = 0.8, (unloading)

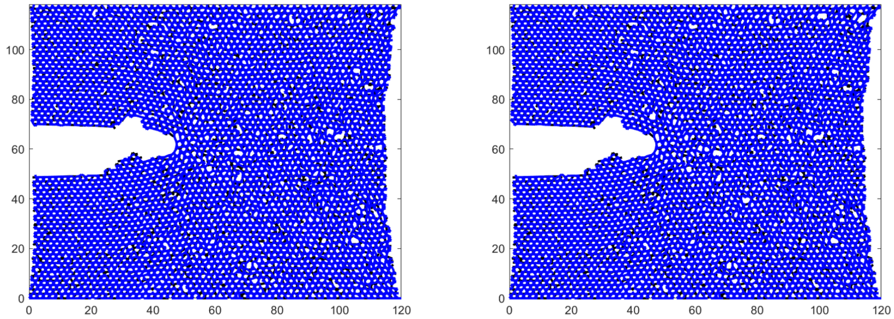

e) p_1 = 0.8, p_2 = 0.8, (loading) f) p_1 = 0.8, p_2 = 0.8, (unloading)

Figure 2.23: Figures show the network plots of loading curves (first column) and unloading curves (second column) in the DN system **with a notch** at the peak stress. Panels (a), (c), and (e) respectively shows the stress vs. strain for $p_1 = 0.65$, 0.7, and 0.8 with a notch.

simulated results for the check of the running program. Fig. 2.18 shows the stress developed in the system with or without the notch. Moreover, Fig. 2.18 highlights the trade-off between the strain at the maximum stress and peak stress. Here, we chose different p_1 such as 0.65, 0.7, and 0.8 to simulate the stiff network near the rigidity percolation threshold, far from it and very far from it.

The simulations of the hysteresis loops with the RPDN model begin with Figs. 2.20 and 2.21. Fig. 2.20 shows that after stretching the double network system up to a strain of 10% of the peak stress, the deformation is irreversible and creates permanent damage in the material. In our model, we allow the bonds to break and buckle, and these mechanisms create hysteresis loops in all combinations of p_1 and p_2. The areas under the curve of the loading and unloading hysteresis curves are important to understand the toughness of the material before and after deformation. In Fig. 2.21, all the panels show an increase in the loading curves' areas, while it is difficult to conclude the areas under the curve of the unloading process.

Lastly, we plotted the network configurations in Figs. 2.22 and 2.23. The results show that at the same stress, which is the maximum, the network configuration pairs (a) and (b), as well as (c) and (d), are different. In both Figs. 2.22 and 2.23, the panels [e and f] produce a similar figure. This is due to the fact that in these figures, p_1 and p_2 are high, and as a result, the system is very rigid. In other cases, the damage in the double network is irreversible. Therefore, the network configurations at the same strain in the loading and unloading curves are not the same.

Chapter 3

Mechanics of Biopolymer Network in Cells

3.1 Cytoskeleton Network

The cytoskeleton is a critical component of the cell. It is responsible for cell shape, cell mechanics, and integrity, and plays an essential role in cell processes such as cell motility and mechanosensing. To perform those tasks, cytoskeleton needs tunability as well as mechanical memory brought by the interactions between actin and microtubule networks. Experimentalists often use in-vitro reconstructions of cytoskeletal networks to study its properties. The work described in this chapter is motivated by such experiments in the Lab of our collaborator Dr. Rae M. Robertson-Anderson and others. In the experiments, microtubules are coupled to 3D acto-myosin networks to obtain actomyosin as an active matter. The experimentalists have shown that using multi-spectral imaging and time-resolved differential dynamic microscopy and spatial image autocorrelation, the ballistic constraction is observed with enough flexible component and motor density. However, a fraction of microtubules is required to have a substained and controlled dynamics. Even though the mathematical model we build does not differentiate the presence or absence of crosslinkers, we shed the light on how the increase concentrations of actin and myosin II motors induced contractility in the double network system. The results are published here [53].

3.2 Model and Method of RPDN (motors)

3.2.1 Motor-Contracted Rigidly Percolating Double Network Model

As mentioned in the previous chapter, rigidity percolation theory has been immensely successful in predicting the mechanical properties and phase transitions in single-component cytoskeletal and extracellular matrix networks as a function of filament concentrations. This theory models biopolymer networks as two interconnected networks of disordered fibers and provides a framework for connecting network rigidity to structure and composition. Here we combine rigidity percolation theory with an active double network model made of a stiff microtubule network and an active semi-flexible actomyosin network. This active rigidly percolating double-network (RPDN) is constructed as follows. Starting with two networks, each based on a fully occupied kagome lattice such that at each crosslink there are no more than two crossing fibers, we dilute the networks by uniformly and randomly removing bonds from the networks according to two different probabilities (Fig. S3). We remove bonds from the stiff microtubule network with probability $1-p_1$ and from the semiflexible actin network with probability $1-p_2$, where $0 < p_1,\ p_2 < 1$, and a contiguous series of colinear bonds constitute a fiber. The stretching moduli of the fibers in the stiff and semiflexible networks are α_1 and α_2 respectively, and the bending moduli are κ_1 and κ_2 respectively. The two networks interact via weak Hookean springs with spring constant α_3, which connect the midpoints of bonds $(x_{\mathbf{1}}, x_{\mathbf{2}})$ and are only present when corresponding bonds are present in both networks. The energy cost of deforming this double network is given by:

$$\begin{aligned}
E_1 &= \frac{\alpha_1}{2}\sum_{<ij>} p_{1,ij}(\mathbf{r}_{ij}-\mathbf{r}_{ij0})^2 \\
&+ \frac{\kappa_1}{2}\sum_{<\widehat{ijk}=\pi>} p_{1,ij}\ p_{1,jk}\ \ \Delta\theta^2_{ijk} \\
E_2 &= \frac{\alpha_2}{2}\sum_{<ij>} p_{2,ij}(\mathbf{s}_{ij}-\rho\mathbf{s}_{ij0})^2 \\
&+ \frac{\kappa_2}{2}\sum_{<\widehat{ijk}=\pi>} p_{2,ij}\ p_{2,jk}\ \ \Delta\beta^2_{ijk} \\
E_3 &= \frac{\alpha_3}{2}\sum p_{1,ij}\ p_{2,ij}(\mathbf{x}_1-\mathbf{x}_2)^2,
\end{aligned} \tag{3.1}$$

where E_1 is the deformation energy of the stiff network, E_2 is the deformation energy of the semiflexible network, and E_3 is the deformation energy of the bonds connecting the two networks. In E_1 and E_2, the first term corresponds to the energy cost of fiber stretching, and the second term to fiber bending [84].

In the above expression, the indices i, j, k refer to sites (nodes) in each lattice-based network, such that p_{ij} is 1 when a bond between those lattice sites is present and 0 if a bond is not present. The quantities r_{ij} and s_{ij} refer to the vector lengths between lattice sites i and j for the deformed stiff and flexible networks respectively, while $r_{ij\mathbf{0}}$ and $s_{ij\mathbf{0}}$ are the corresponding quantities for the initial undeformed networks. Active contractility is incorporated into the semiflexible network by setting the rest length of the bonds in this network to be $\rho s_{ij\mathbf{0}}$, where ρ is a function of myosin concentration as described later in this document and is 1 for a purely actin network and less than 1 for an actomyosin network [5]. The angles $\Delta\theta_{ijk}$ in the rigid network and $\Delta\beta_{ijk}$ in the semiflexible network correspond to the change in angles between initially collinear bond pairs ij and jk for the deformed and undeformed network, respectively. Simulations of the above active RPDN model determined the linear response under 0.005 percent shear. We adopt a shear protocol where external deformations are applied along the top and bottom boundaries and free boundary conditions are used for the left and right sides of the network. For each set of parameters, active double networks containing $\sim 2 \times 10^5$ nodes were randomly generated with given fractions of bonds $1 - p_1$ and $1 - p_2$ missing. The total deformation energy was minimized for the applied macroscopic shear and the shear modulus was calculated as a function of the bond occupation probabilities p_1 and p_2. The values of p_1 and p_2 were obtained from experimental molar concentrations of tubulin and actin respectively, and the contraction parameter ρ was obtained using the ratio of experimental myosin and actin concentrations as described in the next section.

3.3 Calculation

To calculate stretching moduli and bending moduli, we use persistence lengths of 20 m and 1 mm, and diameters of 10 nm and 50 nm, for the actin filaments and microtubules respectively. By defining persistence length l_p as $l_p = \frac{\kappa}{k_B T}$, where κ is the bending stiffness of the bond, k_B is the Boltzmann constant and T is the temperature, the bending modulus is given by the relation $\kappa \propto l_p$. For slender rods, the stretching modulus is given by $\alpha \propto \frac{l_p}{R^{\mathbf{2}}}$, where R is the cross-sectional radius of the rod [50]. From these two relationships, we can calculate the stretching moduli α_1 and α_2, and the bending moduli κ_1 and κ_2, of the fibers in the stiff and semiflexible networks respectively. In our simulations, all moduli are scaled by, and expressed in terms of, α_1. To introduce contraction to the actomyosin network, we assign different values of ρ, or the amount the rest length of each bond is reduced due of myosin-induced contractility2, to networks with different myosin concentrations. We use the Fermi estimate $\rho = 1 - \frac{[myosin]}{[actin]}$, such that in the absence of myosin, the network does not undergo any contraction.

3.3.1 Bond Occupation Probability

Assuming a mesh size of $4.29 \times 10^{(-7)}$ which is 0.429 μm for the actin network,

$$p = \frac{l_0^2[f]N_A}{\lambda_f\sqrt{3}}$$

This relation between the actin and microtubules filament concentrations and the bond occupation probabilities in the semiflexible and stiff networks is calculated and shown in the Supplementary Information of [53]. Similar calculations for collagen and aggrecan concentrations can be done for the previous chapter using this formula.

$$
\begin{aligned}
p_2 &\approx \frac{(4.29 \times 10^{-7})^2 \times 5.8 \times 10^{-3} \times 6.022 \times 10^{23}}{\frac{1}{2.7\times 10^{(-9)}}\times\sqrt{3}} && (3.2)\\
&\approx 1 && (3.3)
\end{aligned}
$$

For the microtubule network, the mesh size is assumed to be $7.33 \times 10^{(-7)}$ which is 0.733 μm,

$$
\begin{aligned}
p_1 &\approx \frac{(7.33 \times 10^{-7})^2 \times 5.8 \times 10^{-3} \times 6.022 \times 10^{23}}{\frac{13}{12} \times 10^{(-9)}\times\sqrt{3}} && (3.4)\\
&\approx 1 && (3.5)
\end{aligned}
$$

The actin concentrations were changing as 0.25,0.5 and 0.75 percentage of 5.8μM. Therefore, p_2 are 0.25, 0.5 and 0.75. Meanwhile, the microtubule bond occupation probabilites are 0.75, 0.5 and 0.25.

3.3.2 Stretching and Bending Rigidity

The current calculation is based on the underlying assumptions on the parameters:

- The persistence length of actin is $l_{p,actin} \quad \approx \quad 20 \quad \mu m$
- The persistence length of microtubule is $l_{p,MT} \quad \approx \quad 1 \quad mm$
- The diameter of actin filament is $d_{actin} \quad \approx \quad 10 \quad nm$
- The diameter of microtubule filament is $d_{actin} \quad \approx \quad 50 \quad nm$

Here we are finding the ratio of the bending modulus of microtubule over the stretching modulus of microtubule :

$$\begin{aligned}
\frac{\kappa_{MT}}{\alpha_{MT}} &\approx \frac{l_{p,MT}}{l_{p,MT}/a_{MT}^2} \\
&\approx a_{MT}^2 \\
&\approx (\frac{a_{MT}}{\eta_{MT}})^2 \\
&\approx (\frac{25 \times (10)^{-9}}{7.33 \times (10)^{-7}})^2 \\
&\approx 1.2 \times (10)^{-3}
\end{aligned}$$

For the ratio of the bending modulus of actin over the stretching modulus of microtubule :

$$\begin{aligned}
\frac{\kappa_{actin}}{\alpha_{MT}} &\approx \frac{(l_{p,actin})}{(\frac{l_{p,MT}}{a_{MT}^2})} \\
&\approx (\frac{l_{p,actin}}{l_{p,MT}})(\frac{a_{MT}^2}{\eta_{actin}^2}) \\
&\approx (\frac{20 \times (10)^{-6}}{1 \times (10)^{-3}})(\frac{25 \times (10)^{-9}}{4.29 \times (10)^{-7}})^2 \\
&\approx 6.8 \times (10)^{-6}
\end{aligned}$$

For the ratio of the stretching modulus of actin over the stretching modulus of microtubule :

$$\begin{aligned}\frac{\alpha_{actin}}{\alpha_{MT}} &\approx \frac{(\frac{l_{p,actin}}{a^2_{actin}})}{(\frac{l_{p,MT}}{a^2_{MT}})} \\ &\approx (\frac{l_{p,actin}}{l_{p,MT}})(\frac{a^2_{MT}}{a^2_{actin}}) \\ &\approx (\frac{20 \times (10)^{-6}}{1 \times (10)^{-3}})(\frac{25}{5})^2 \\ &\approx 0.5\end{aligned}$$

These are all the parameter values used in our simulations.

3.3.3 Contractility

Lastly, we found the contractility parameter ρ as below.

$\rho = (1 - \frac{[Myosin]}{[Actin]})$	Myosin (μM)	Actin (μM)	$\frac{[Myosin]}{[Actin]}$
0.92	0.12	1.45	0.08
0.83	0.24	1.45	0.17
0.67	0.48	1.45	0.33
0.96	0.12	2.9	0.04
0.92	0.24	2.9	0.08
0.83	0.48	2.9	0.17
0.97	0.12	4.35	0.03
0.94	0.24	4.35	0.06
0.89	0.48	4.35	0.11

3.4 Results

Our collaborators create an actin-microtubule network with myosin II motor proteins, image it by using multi-spectral confocal microscopy and utilized differential dynamic microscopy (DDM) and spatial image autocorrelation (SIA) to find the quantitative qualities for the active system. Even though the system is a spatiotemporally varying active composite, we analyze the steady state behavior using our RPDN simulations with motors. Using results from the simulations of active biopolymer double network, we find some correlations between measured restructuring dynamics and the mechanical properties of the quasi-static system from the model.

As mentioned in the introduction of this chapter, we change the molar actin fraction ϕ_A with the combined concentration of actin and tubulin as a constant in order to find the fraction of actin required to have a controlled dynamics. Moreover, we change the molar myosin concentration c_M from 0.12-0.48 μM and observe the dynamics of the network over the long period from approximately 45 minutes to several hours. Even though the protein concentrations used in the experiments are less than those present in cells, our parameter space is explored and improved [27, 54, 79] over various trial and error runs in the previous in vitro studies of actomyosin and actin-microtubule network as a potential system for tunability and resilience.

First, we showed the experimental and simulated double network of actin and microtubule with motor induced contractility in Figure 3.1. Increasing molar actin fraction ϕ_A and myosin concentration c_M generally exhibits in larger degree of contraction and restructuring in both of the results of experiments and simulations. We calculated the shear (elastic) modulus G' in simulation units using the expression

$G' = \frac{2\epsilon}{\gamma^2}$, where ϵ is the minimized energy per unit corresponds to 210 kPa. We use this conversion to obtain the values of G' presented in Figure 3.2. Since our simulations assume physical crosslinking in the microtubule and actin networks (absent in experiments), we believe that our simulations overestimate the true value of the modulus.

3.5 Discussion

The combined results of experiments and simulations have provided an analysis of the dynamics, structure, and mechanics of the myosin-driven actin-microtubule system with respect to the concentration of each protein, shedding light on the possibility of inventing a cytoskeleton composite that allows for tunable and resilient active materials. Our results are novel as previous studies have focused on crosslinked actomyosin as a soft matter system, whereas we show that coupling microtubules to actomyosin systems provides a phase space with desirable emergent and useful properties for cytoskeleton-inspired synthesis in comparison with other single-substrate systems. Our comprehensive phase map provides the general design principles of active and adaptable double network materials with some form of contractility for robust actomyosin contraction. These rules can be applicable in wound healing, filtration, and soft robotics. Importantly, our work demonstrates that different dynamical and structural properties arise by changing the relative concentrations of actin, tubulin, and myosin inside the cell. The phase map summarizes that more contractility can be achieved in the composite by increasing myosin and actin while the rigidity is brought by adding more connectivity and microtubules.

To mimic the behavior of the cell, composites with more filaments and different microtubule lengths, crosslinkers, and microtubule-associated kinesin motors can be studied in future work. From a modeling perspective, this model simplifies that the crosslinking of both networks is permanent and does not incorporate time evolution, viscous dissipation, or filament bundling.

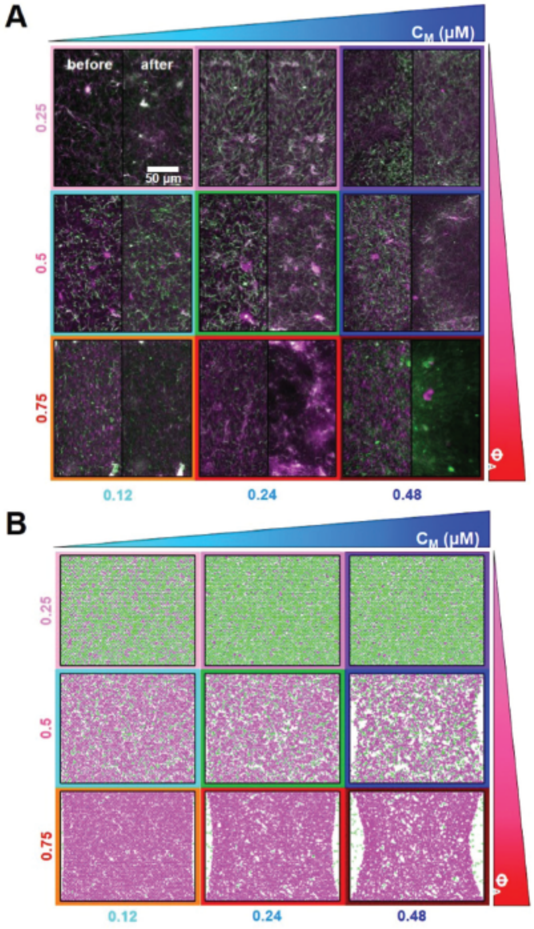

Figure 3.1: Varying the composition of active cytoskeleton composites (A) 256 x 128 pixel (212 x 106 μm) two-color confocal microscopy images show how the actin filaments (magenta) and microtubules (green) are restructuring and rearranging with myosin II motor activity. Each panel, left images are taken at the beginning of the experiment and the right images after. The order of the panels are arranged by increasing molar fraction of actin ϕ_A from top to bottom colored in red and myosin concentration $c_M$in blue from left to right. The box color match the color coding in the elastic modulus figure. (B) A simulated double network with motors deform for different concentrations of myosin and actin. The size of the simulation box is 88 x 73 μm.

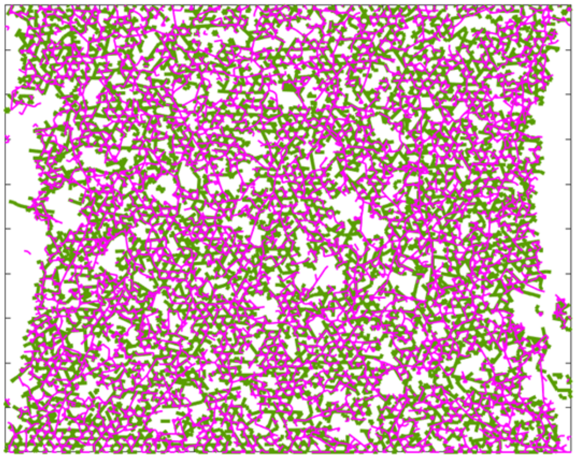

Figure 3.2: Model of an active double-network with molar actin fraction $\phi_A = 0.5$. Actin filaments are shown in magenta and microtubules are shown in green.

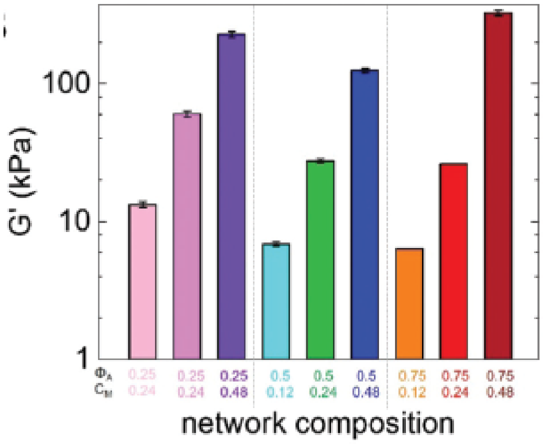

Figure 3.3: Elastic modulus G' of an active double networks with the parameters ϕ_A and

Chapter 4

Biophysics of Viral Life Cycle and the response to therapeutics

4.1 Viral Life Cycle

In the evolution of viruses, especially in error-prone RNA viruses, the interplay of mutation, replication, and other selection processes lead to populations of viruses, known as viral quasispecies, with similar sequences but a distribution of genomes [44]. Statistical mechanics of viral quasispecies provides a framework to understand how a virus survives the immune clearance system and provides insights into the population biology of viruses. In addition, studying quasispecies dynamics can suggest approaches for developing antivirals because the viruses can be considered "moving targets" when replicating [70]. In this work, we use this framework to systematically study the impact of different anti-viral therapeutic strategies that target different

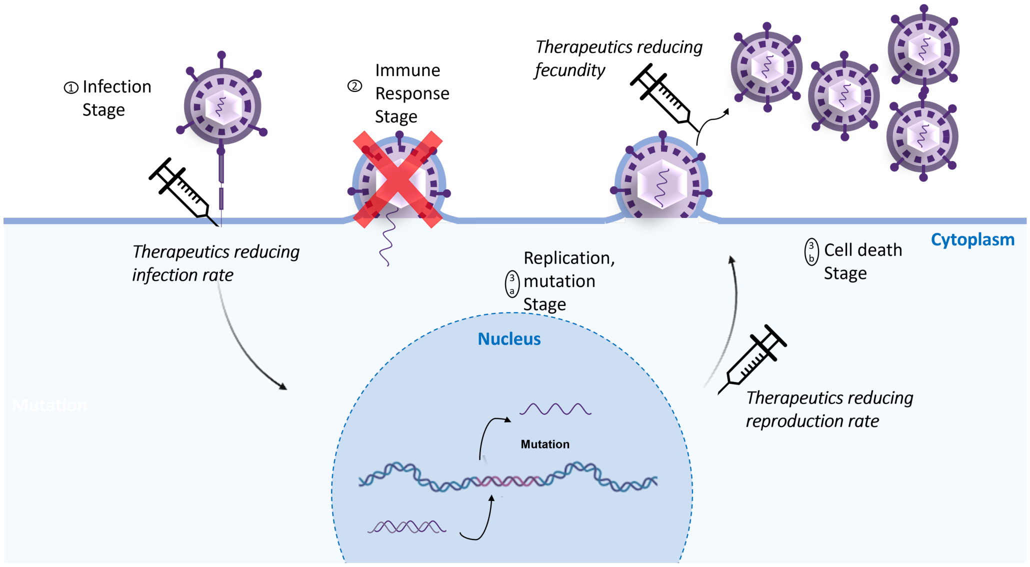

Figure 4.1: **Application of therapeutics at different stages of the viral life cycle.** A simplified schematic showing the life cycle of a virus and anti-viral therapeutics targeting different stages of the cycle. We modeled the actions of the therapeutics as lowering of the infection rate, fecundity, and reproduction rate, and calculated the virus population in the bloodstream and inside cells.

aspects of the life-cycle of respiratory viruses such as influenza, cold viruses and particularly SARS-CoV-2. We build on previous studies [42, 55] that model the viral life cycle as three main discrete stages of infection, immune clearance and replication, and investigate the aftermath of administering antivirals at a specific time after first infection, that selectively reduce the infection rate, the replication rate, or the fecundity of the virus, where we define fecundity as the maximum number of new viruses that can be produced from each progenitor virus. Although we are investigating a general rule for a broad class of viruses, the results provide useful insights on which part of the viral cycle to focus on to produce the most effective antiviral therapeutics.

Antivirals work by disrupting specific aspects of the viral life-cycle and can be generally categorized based on their strategy [28]. Inhibitors of viral RNA polymerase or RNA transcriptases may be able to reduce the reproduction rate or fecundity of viruses [91]. Therapeutics can also interrupt viral protein synthesis by inhibiting viral proteases, which is an essential step in viral assembly and replication [96]. Proposed and existing therapeutics include CRISPR-Case-based Gene Therapy [41], defective viral genomes (DVGs) [102], monoclonal antibodies and other protease inhibiting antivirals [49, 52, 57, 64, 90, 93]. Other antivirals may restrict the entry of viral protein into the nucleus thereby reducing the reproduction of viruses [37]. Alternatively, other viral entry inhibitors may restrict viral entry into the cell by preventing membrane fusion or endocytosis [96], [92], [47]. These types of antivirals may be able to change the probability of cellular infection. Note that the above-mentioned types of antivirals are not necessarily proven effective for Covid-19 patients. Here we consider examples of different types of antivirals affecting fecundity, reproduction and infection rates, as shown in Figure 4.1.

There have been numerous modeling efforts focused on understanding and incorporating different facets of viral infection in the context of therapeutics, and we summarize some key classes of them here. Early models centered around within-host viral kinetics (VKs) and studied the time evolution of uninfected and infected cells with virions [10, 31]. These models were initially used in studying HIV-1 infections [72] and were later extended to other viruses. Moreover, PK/VK models incorporating pharmacokinetics (PK) dynamics have been developed to study antiviral effectiveness [56, 65, 98], such as in the study of alisporivir interferon-free treatment in hepatitis C virus infected patients [33]. Similar models are also being used in studying Covid-19 disease dynamics [14, 38, 71]. In addition to the mechanistic approaches mentioned above, more data-driven methods for learning about SARS-CoV-2 variant binding strengths are being carried out through simulations [11]. Lastly, for Model Informed Drug Development (MIDD), some other modeling efforts [13, 20] involve using Quantitative System Pharmacology principles (QSP).

In our model, we consider an iterative procedure, shown in Figure 4.1, in which a virus first attempts to infect a cell from an environment composed of a distribution of viral types. We discuss more about this distribution, a quasi-species distribution, below. If the virus is successful in infecting the cell, it is next exposed to the host immune system. Any surviving viruses then have a probability of reproducing with a fixed fecundity, with each viral offspring given a random mutation in one codon. These new viruses then escape into the environment, and go on to try to infect other cells.

In our model system, the cells are all identical, with a protein receptor “lock” 50 codons (AA) long. Each codon takes a value from A-Z, with a fixed pattern for the cells of a 50-character sequence. The viruses, on the other hand, have a “key” receptor-binding protein that is 100 codons long, again with each taking the 26 possible values A-Z, but for the viruses the values are variable, allowing 26^{100} different possible viruses. In modeling the infection process, we conceptually mimic the binding process whereby a virus attaches to a cell as the virus aligning its “key” with the cell’s “lock”, sliding its 100 codons along the lock and testing at each alignment how many codon matches there are. The alignment with the greatest number of matches of virus to cell has a number of matches we term the “match number" for that virus, and, in our model, is the identifier for that virus. Because of the differing sequence lengths of codon regions between virus and cell, the match number can range from 0 to 50, giving 51 different values.

As the viruses enter from the environment and begin engaging in the infection process, they hop from cell to cell, at each trying to infect. If a cell is already full, the virus cannot infect and must hop to the next one. If after trying all cells the virus cannot infect, it is considered to have left the active region of the host. The probability of a virus entering a cell on a given hop, if the cell is not full, is e_m, where $e_m = \exp\left(\frac{-(50-m)}{T}\right)$. Here m is the match number for the virus attempting to infect, and T is a parameter we term cell permissivity, a measure of how easily a virus with fixed match number can replicate. For low permissivity, the match numbers need to be near 50 to infect, while for high permissivity, a broad range of viruses are able to infect. The net result of the hopping and probabalistic infection of N successive viruses from the environment, with the fixed number of cells gradually filling up as the later viruses try to infect, is an updated infection probability of the cells, and a new distribution of viral match numbers within the cells, that we term $\psi^I(m)$. This is expressed in a recursive formula which is described in the (Details) sessions.

The second stage or the energy barrier to overcome for the virus after infection is the immune response, Ξ_m. It is modeled as a sigmoid, which will generate a high immune response for any virus with more than a few matches, $\Xi_m = \frac{A}{1+\exp\left(\frac{-(m-\nu)}{2}\right)}$. The immunity parameter A is varied between 0 and 1, while the onset parameter ν has been suggested to be set to 6, as a typical epitope length [1]. Therefore, Ξ_m will approach 1 when m is toward the midpoint of the unit interval, and A is 1. The cell occupancy distribution after the immune response is calculated using the above-mentioned sigmoid function, $\psi^{\Xi}(m) = \psi^{I}(m)(1 - \Xi_m)$. While infection increased the number of viruses in the cells, the immune response decreases the number of viruses in the cells, and again changes the distribution of m in the cells. Note that infection and immune response induce opposing pressures on a virus, one for higher match number to infect, but then needing low match number to escape the immune process.

The final stage is the reproduction stage, where the viruses in the cells have a probability based on their match number to reproduce and mutate. We take the probability to reproduce to be e_m. Then the viruses left in the cells can be expressed as $\psi^{R}(m) = \quad \psi^{\Xi}(m)(1 - e_m)$. Conversely, the probability of the virus producing an offspring successfully is $\psi^{F}(m) = e_m \psi^{\Xi}(m)$. We set the fecundity to be $f_0 = 20$, and for each viral offspring, exactly one of the 100 codons is randomly changed. This mutation can result in the virus having a new match number which is either one greater than before, one less than before, or unchanged. These probabilities are different for every m (more likely to increase for small m, more likely to decrease for larger m), and the net we express as a mutation matrix is applied to each probability vector $\psi^{F}(m)$. This new cohort of reproduced viruses then composes the viral environment for the next iteration. The number of viruses in the environment for each m is $cf\psi^{F}(m)$, where c is the number of cells and f is the fecundity. Each iteration is taken to be one-time step. Iterations are repeated until a steady state is achieved. By varying immune strength A and cell permissivity T over a full range, a phase diagram can be obtained.

We use this framework discussed above to examine three strategies for anti-viral therapeutics: reduction of infective ability, reproductive ability, and fecundity. To reduce the reproduction rate and fecundity, we multiply the previously defined $\psi^F(m)$ and f by scaling prefactors R and F respectively, with R and F ranging from 1 (no therapeutic) to zero. To reduce the infection rate, we multiply the part of the infection process that has to do with the ability to enter the cell by a scaling prefactor I ranging between 1 and 0. Details of how this is implemented are in the Supplementary Information. Every simulation starts at time $t = 0$ with the parameters I, R, and F set to unity, and then at the point $t = 10$ one or the other of the three anti-viral parameters is set to a value less than one and kept fixed at this value, indicating the continuous dosing of a therapeutic. The simulation is continued until a steady state is reached, in which either the virus is extinct (successful therapeutic) or a steady state nonzero level of virus remains. We vary the reduction parameters I, R, and F over a range of values between 0 and 1, and we choose four characteristic points on the phase diagram (sets of parameters A and T) to have a sampling of hosts with both low and high immunity, and low and higher cell permissivity.

The full phase space of the model discussed in this work has three main phases of infection type: acute, opportunistic, and chronic [55]. Here we focus on the acute phase representing respiratory diseases including flu, SARS, and in particular COVID-like diseases. Within this phase, we sample from four different locations as shown in Figure 4.2(c). The corresponding four sets of permissivity (T) and immunity (A) used are ($T = 0.5$, $A = 0.2$), ($T = 0.5$, $A = 0.5$), ($T = 0.5$, $A = 8$) and ($T = 12.9$, $A = 0.5$). We choose three locations at the same permissivity of $T = 0.5$

which is in the middle of the phase. The last point we choose is at the permissivity of $T = 12.9$ and immunity of $A = 0.5$.

4.2 Results

4.2.1 Targeting Fecundity

First, we discuss the effect of lowering fecundity through therapeutics as shown in Fig. 4.2. The viral population in the bloodstream, also called the viral load, decreases linearly with the decrease in fecundity, $f_0 - f$, in all cases studied (Fig. 4.2a). The viral population in the cells is initially much smaller than in the bloodstream and stays almost steadily constant as the fecundity is reduced; however, it goes to zero (extinct virus) at the same level of therapeutic as that for the viral population in the bloodstream ((Fig. 4.2b). The viral population both in the bloodstream and inside cells is the smallest for the case where the immunity is highest and the permissivity is lowest ($A = 0.8, T = 0.5$), and it reaches zero for a smaller reduction in fecundity for this case, compared to all other cases. For a fixed permissivity ($T = 0.5$), the viral populations increase with decreasing immunity, A, as expected. For fixed immunity ($A = 0.5$), the dependence on permissivity, T, does not show a clear, monotonic trend (See Supplementary Information). We also calculated the order parameter, defined as the normalized sample mean of the environmental (blood stream) match number distribution, in the parameter space of immunity and permissivity for high ($f = 20$) and low ($f = 9$) fecundity. We find that the region of parameter space over which the virus goes extinct grows as the fecundity is reduced as shown in Figs.

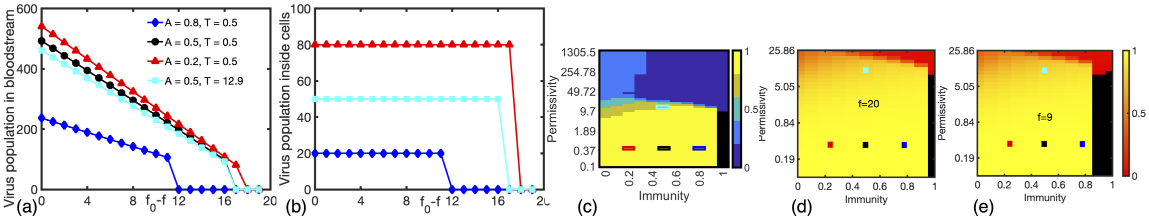

Figure 4.2: **Relationship between virus populations and the change in fecundity f.** (a) Virus population in the bloodstream and (b) virus population inside cells at steady state as a function of the change in fecundity, $f_0 - f$ following the application of the antiviral. (c) Heat map of the order parameter showing distinct regions for acute, chronic and opportunistic phases, similar to [55]. The four rectangular boxes in red, black, blue and cyan show the four cases studied in this paper, which focus only on the acute phase (yellow in (c)). Figure (d) shows the heat map of the order parameter for a control sample where no antiviral is used and figure (e) for the case where the antiviral is administered; both heat maps have the same color-scale. The region of parameter space with where the virus has gone extinct is shown in black in the heat map.

4.2d and 4.2e. However, those specific regions of phase space for the parameters we discussed above do not show a significant change in order parameter.

4.2.2 Targeting Reproduction Rate

To understand the impact of antivirals which lower the probability of reproduction of viruses, we changed the reproduction rate of the system, R, after 10 time steps. At the default value of $R = 1$, i.e., before the anti-viral is administered, the case with the lowest A and the lower T generates the largest viral load in the environment. As with fecundity, we observed a reduction in the viral population in the bloodstream as we decrease the reproduction rate, R, for all cases (Fig. 4.3a), while the viral population in cells initially stays constant as R is decreased but drops to zero at the same time as the viral population in the bloodstream (Fig. 4.3b). The decrease in

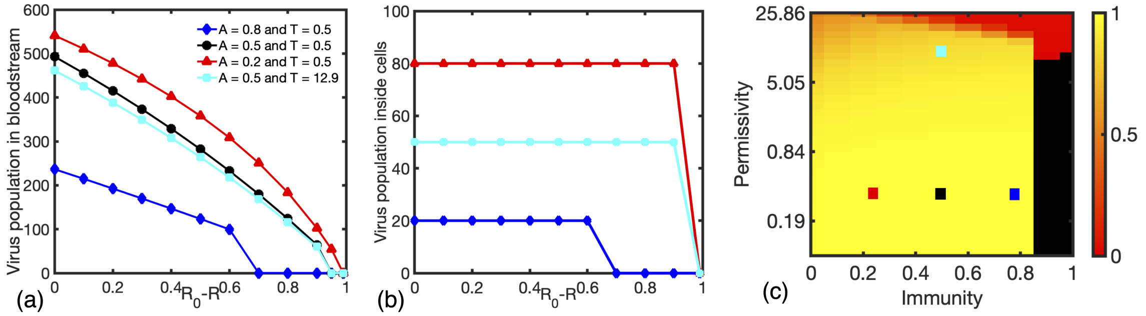

Figure 4.3: **Relationship between virus populations and the change in reproduction rate R. (a)** The virus population in the bloodstream and (b) in the cell at steady state as a function of the change in the reproductive rate, $R_0 - R$. (c) The heat map of the order parameter shows an increase in the area of extinction when the viral reproduction rate is reduced. Extinct viruses are marked with a black color on the heat map. All heat maps have the same color scale.

the viral population in the bloodstream, however, follows a non-linear relationship with $R_0 - R$, in contrast to decreasing fecundity (Fig. 4.3a). This non-linear scaling is the most noticeable for the case of $A = 0.2$ and $T = 0.5$, when viruses have the least resistance from these pressures. The order parameter heatmap for the reduced reproduction rates show an increase in the extinction region as in case of reducing fecundity (Fig. 4.3c).

4.2.3 Targeting Infection Rate

We investigate the impact of antivirals which target the rate of infection by implementing a reduction in the infection rate at time $t = 10$ in our simulations. The resulting impact was unexpected and different from the antivirals that had targeted fecundity and reproduction rate. Specifically, the viral population in the bloodstream changes non-monotonically as we decrease the infection rate, first increasing

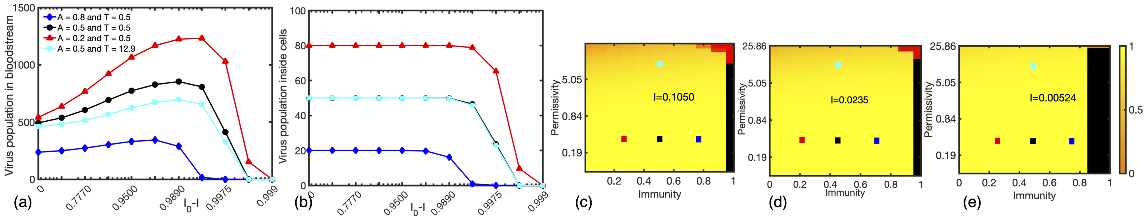

Figure 4.4: **Relationship between virus populations and the change in Infection Rate I.** **(a)** The virus population in the bloodstream and **(b)** in the cell at steady state versus the reproductive rate I changed to after the tenth time step. The antiviral reducing infection rate shows significantly different trends in all cases. **(c)**,**(d)**, and **(e)** Phase diagrams with various levels of therapeutic. Extinction regions are marked with a black color on the heat map. The chosen infection rate is indicated on each heat map.

and reaching a maximum which can be quite prominent, and then decreasing and finally going to zero i.e. going extinct, as shown in Fig. 4.4a. We conjecture that this initial increase takes place because even though a decrease in infection rate leads to fewer viruses in cells, these viruses now face less competition and are able to reproduce and evade the immune system, leading to a higher rate of reproduction, effectively leading to an initial increase in the viral load. This initial increase in the viral load is largest for the case of the lowest immunity $A = 0.2$. The change in the viral population inside cells follows qualitatively similar trends in this case as with the reduction in fecundity and reproduction rate (Fig. 4.4b). For both viral populations in the bloodstream and in cells, for higher immunity, viral extinction requires smaller reductions in infection rate (Fig. 4.4a and 4.4b). This is also observed in the heat map of the ordered parameter, for the cases $I = 0.1050$, $I = 0.0235$, and $I = 0.0052$ shown in Fig. 4.4 c,4.4 d, and 4.4 e).

Viral quasispecies dynamics for different anti-viral strategies

We show a comprehensive analysis of the impact of the therapeutics in terms of the evolution of the viral population, match number, and the quasi-species distribution in Fig 4.5. For antivirals that reduce the fecundity and reproduction rate, for the case of high immunity, the viral load drops to a value close to zero after the antiviral is administered and remains there (Fig. 4.5a and 4.5e), while for the case of low immunity although the viral load drops right after the antiviral is used, it does not go to zero, and reaches a non-extinct steady state (Fig. 4.5b and 4.5f). No clear mutations in the quasispecies distribution are observed (Fig. 4.5c, 4.5d, 4.5g, 4.5h). Our results for the time dependence of viral load for fixed values of infection-reducing therapeutic chosen at two characteristic values in the rise and fall show that the viral load increases quite quickly after the therapeutic is implemented for high immunity(Fig. 4.5i), but show an extended rise over time for the lower immunity (Fig. 4.5j and 4.5n). The only time this trend is reversed and we see a decrease is for the case that combines high immunity ($A = 0.8$) with low permissivity ($T = 0.5$) and low infection rate ($I = 0.00524$) (Fig. 4.5m). A possible explanation for the rise in viral load with implementation of infection-lowering therapeutic is suggested by the studies of quasi-species distribution as a function of time, showing a set of mutations, most prominently seen in Figures 4.5l and 4.5p, to higher match number. These mutations allow the virus to reproduce more. Although the mutations do not appear particularly large, the e_m function governing reproduction is an exponential function of the deviation of the viral match number from $m = 50$. As a result, we see the virus population increasing. We provide more details.

Finally, we examined how the viral population in the bloodstream and in cells changed over time in response to antiviral therapeutics that lowered the fecundity, the reproduction rate, and the infection rate, for the cases of high and low immunity. In Fig 4.6, $F = 0.05$, $R = 0.01$ and $I = 0.0015$ are selected to show how the virus population in both bloodstream and cells approach extinction. As seen in the figures in the first column (Figs. 4.6a, 4.6c, 4.6e), with the high immunity $A = 0.8$, the viral load reduces abruptly; therapeutics and high immunity work together to eliminate viruses. However, with the low immunity $A = 0.2$, as shown in the figures in the second column (Figs. 4.6b, 4.6d, 4.6f), viruses stay inside the cells for dozens of our time units, which depending on the virus can correspond to days or even weeks, before the viral population approaches a tiny number, if it does. As shown for the therapeutic affecting infection, even at a reduction of the ability to enter a cell to 0.1 percent of its full value, the virus does not go extinct, and in fact rises with time up to its steady state value. In the SI we show the reduction of infection to 0.00524 still does not clear the virus for the low-immunity case. The time delay of viral extinction in the bloodstream and inside cells might provide valuable contributions to discussion about the long-term nature of illness.

4.3 Discussion

We investigate the efficacy of antivirals in terms of their ability to reduce the fecundity, the reproduction rate and the infection rate of viruses by implementing the change in the respective parameters after a certain number of iterations, representing

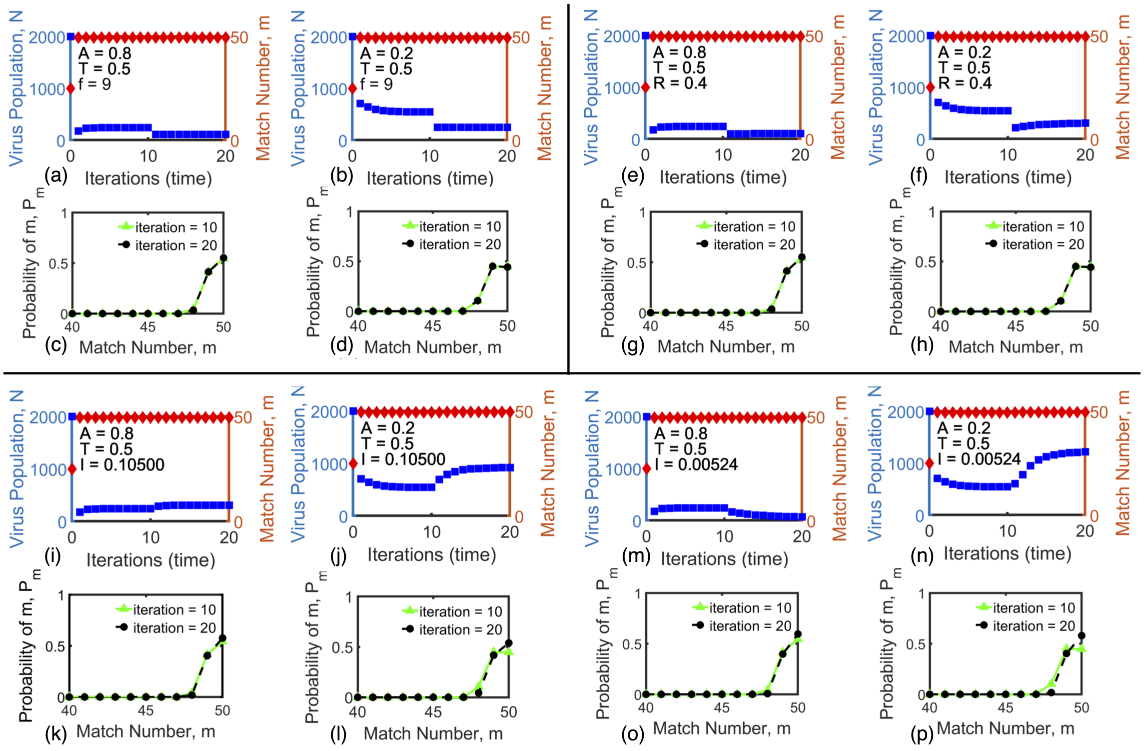

Figure 4.5: **The virus population and the probability of matches for given permissivity and immunity for antivirals targeting the fecundity, reproduction rate, and infection rate** Figures (a)-(d) show the impact of varying the fecundity (lowering it to $f = 9$), figures (e)-(h) the results of varying the reproduction rate (lowering it to $R = 0.4$), and figures (i)-(p) show the results of varying the infection rate (lowering it to $I = 0.10500$ for (i)-(l), and to $I = 0.00524$ for Fig. (m)-(p)). The virus population in the bloodstream (viral load, blue) and average match number (order parameter, red) are shown in Figs (a),(b),(e),(f),(i),(j), (m), and (n), and the quasispecies distributions before and after the therapeutic is administered are shown in Figs. (c), (d), (g), (h), (k),(l)(o),(p); data shown in green correspond to times prior to application of therapeutics, and data shown in black represent the effect of adding therapeutics. The permissivity is kept fixed in all cases at $T = 0.5$. Figs (a),(c),(i),(k),(e),(g),(m),(o) show results at a high value of immunity $A = 0.8$, while Figs. (b),(d),(j),(l), (f),(h),(n),(p) show results at a low value of immunity $A = 0.2$. Note that no clear mutations in the quasispecies distribution are observed for the cases of lowering fecundity or reproduction rate, however for antivirals that lower the infection rate, mutations in the quasi-species distribution are observed with a shift to higher match numbers enabling higher reproduction rate, particularly for lower immunity.

a time delay from first infection to feeling sick enough to seek medical intervention. As expected, an antiviral that leads to a fewer number of offspring per virus, i.e. a smaller fecundity, leads to a decrease in the viral load. This effect is monotonic, and the number of viruses at a given time is a linear function of the change in fecundity; this is a desired behavior because it allows to predict the impact of the antiviral with consistency, including to infer the data in the regions parameter space we do not show in the manuscript. For the therapeutics reducing the reproduction rates of the viruses, once again the viral load decreases smoothly monotonically with the decrease in the reproduction rate, but this decrease is linear only for the case of high immunity and low permissitivity ($A = 0.8, T = 0.5$). An example of an antiviral that reduces the reproduction rate is Paxlovid [2], which combines, nirmatrelvir, a protease inhibitor which interferes the reproduction process, and ritonavir, which makes sure nirmatrelvir is not metabolized away easily [1]. The success of this antiviral in preventing progression of the disease and reducing hospitalization agrees with our results on the effectiveness of antiviral strategies that target the reproduction rate of viruses.

The impact of antivirals that lower the ability to infect was intriguing and somewhat counterintuitive. We saw that the viral load changed non-monotonically with the decrease in infection rate, initially increasing, reaching a maximum, and then decreasing. We conjecture this initial increase to be due to less competition faced by the viruses already successful in infecting the cell, their unrestricted reproduction, and potential mutations; the latter is suggested by the shift to increased match number of the quasi-specicies distribution when the therapeutic is administered. These effects combine leading to an accumulation of viruses in cells, with the viruses reproducing until all the cells are empty and devoid of viruses, which critically depends on the level of immunity. There are examples of antivirals with a similar strategy, which despite their reported ability to reduce the infection rate of a wide range of viruses, were found to be not be very effective in mitigating Covid -19 in patients [9]. This is likely because, as our results highlighted, reducing the infection rate is not effective in reducing the overall viral load if the viruses continue to replicate, and potentially mutate.

One question left is what defines and quantifies the illness or symptoms of the viral infection. If the viral load is reduced in the bloodstream but most cells are still filled with viruses, there is a possibility that the patient may still suffer from the symptoms of the viral infection. For Covid-19, many patients report the long haul struggle with the symptoms such as trouble breathing, muscle aches and chronic fatigue [60]. Despite the fact that hypotheses for the causes of "long COVID" range from blood clots [78, 100] to immune abnormalities [15], some research suggests that antivirals would be a solution to eliminate the reservoir of viruses inside cells [51]. Our model also shows the slow approach of the viruses inside the cells to extinction under therapeutics. The extinction rate depends on the strength of the applied therapeutics and also very much on the immune strength.

Individuals in our model with high immunity not only get well, but get well rapidly after a therapeutic is administered (See Fig. 4.6 a,c and e). For individuals in our model with a weak immune response, as shown in Fig. 4.6 b and d, reducing the fecundity and reproduction rate to a very small number, which is equivalent to administering a strong therapeutic, brings the virus population in the bloodstream within a few iterations to extinction. However, there is a much longer time scale to clearing the virus from the cells for those with low immunity, extending to 20-30 iterations (approx. 20-60 days). Also, as Fig. 4.6 f shows, for some therapeutics, even a strong dose for those with low immune response fails to clear the virus from either blood stream or cells. In summary, those with weaker immunity not only don't always get their virus cleared if the therapeutic is not strong enough, but also, most tellingly, have a very long time scale to the removal of virus from their cells. Since it is viruses in cells that activates the immunity, our results may give insights to the causes of both exaggerated immune response.

4.3.1 Simulation Details

The simulations are performed on Rochester Institute of Technology's Hight Performance Computing (HPC) cluster, named SPORC (Scheduled Processing On Research Computing). With the help SLURM manager and the capacity of the cluster, each task for each simulation of permissivity T and immunity A combination is run efficiently. The system size is defined by maximally 2000 number of viruses attempting to infect 100 empty cells for 400 iterations. The convergence is shown by reaching the steady state values in the number of viruses in the environment.

4.3.2 Mathematical model (Details)

We explain the details of the viral life cycle models we used in the previous session. There are three different stages of a viral life cycle we simulated - infection, immune

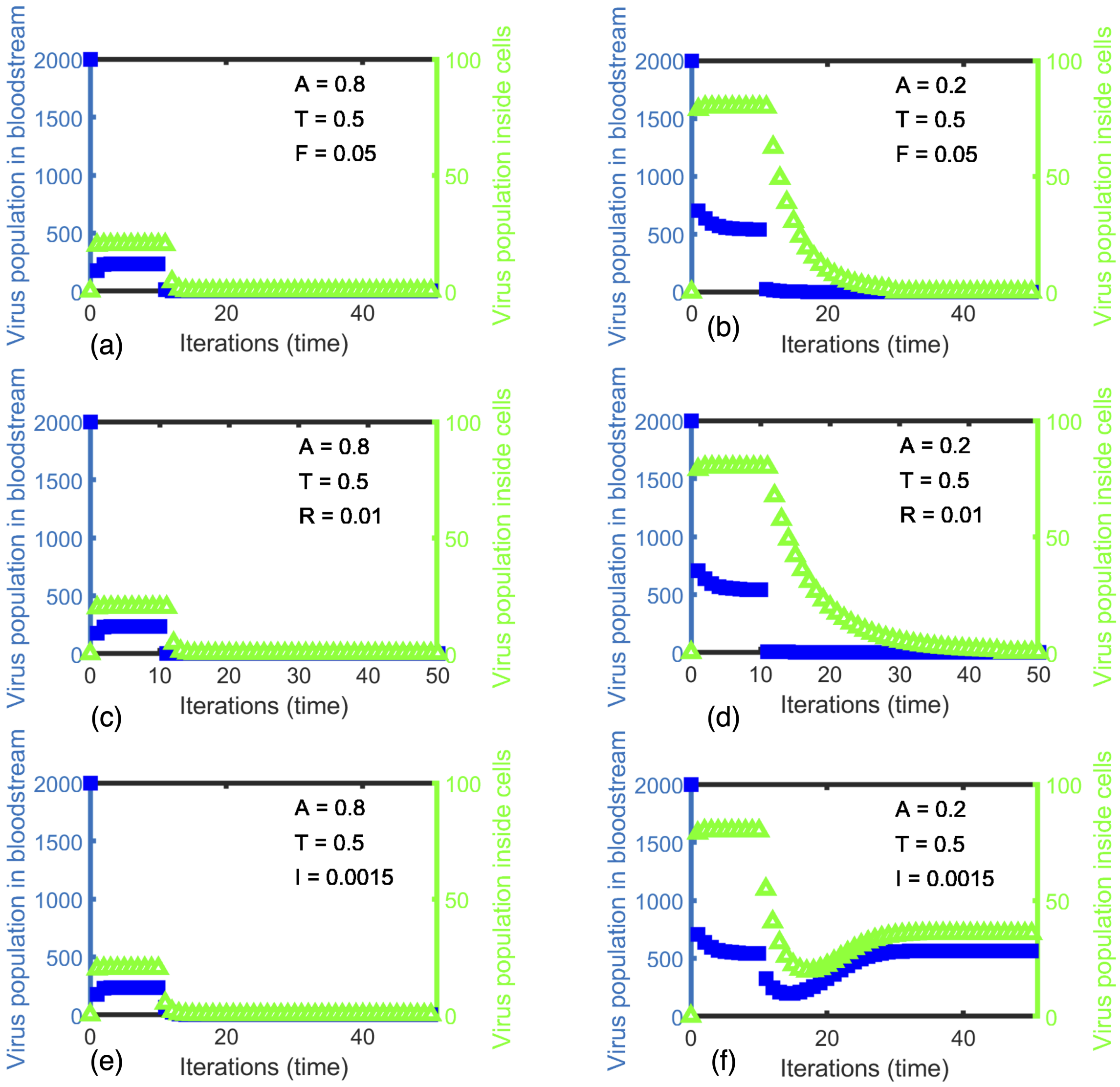

Figure 4.6: **Time-dependent comparison of virus population in bloodstream vs inside cells at extinction.** The virus population in the bloodstream plotted in blue (right y-axis) and inside cells plotted in green (left y-axis). Permissivity $T = 0.5$ in all cases. Immunity $A = 0.8$ for the left columns (a), (c), (e) and Immunity $A = 0.2$ for the right columns (b), (d), (f)

clearance and reproduction. We calculate the probability distribution of viral quasispecies in each stage with or without the applied therapeutics.

The probability distribution of match numbers in the cells after infection by a quasi-species distribution of viruses is calculated as follows. In our model the virus quasispecies distribution infects via viruses emerging from the blood stream, and attempting to infect cells, hopping across cells, trying to infect one cell at a time. At each cell, there are two constraints: the first is related to the cell permissivity, represented by $e_{m(infect)}$, and second to whether the cell is already infected and occupied and this is represented by the sum over all m of the quasispecies present in the cell prior to virus k arriving, or $\sum_{m'} \psi^I_{k-1}(m')$. Both of these quantities are between 0 and 1, representing probabilities. The probability that the virus will find the cell empty enough to enter is then $1 - \sum_{m'} \psi^I_{k-1}(m')$, and the combined probability to infect a cell in a single attempt is the product of the two, $e_{m(infect)}(1 - \sum_{m'} \psi^I_{k-1}(m'))$.

The probability of the virus encountering all c cells and infecting at most one cell is expressed as one minus the probability of encountering all c cells and not infecting any one of them, or $[1 - [1 - e_{m(infect)}(1 - \sum_{m'} \psi^I_{k-1}(m'))]^c]$. We average over all cells and the full viral quasispecies distribution. The net distribution in the cells after the k^{th} virus has tried to infect is then the distribution after the encounter with the $(k-1)^{th}$ virus plus the new infection attempt from virus k. This distribution is shown in the following equation:

$$\psi^I_k(m) = \frac{P_m}{c}[1 - [1 - e_{m(infect)}(1 - \sum_{m'} \psi^I_{k-1}(m'))]^c] + \psi^I_{k-1}(m)$$

This process repeats until all N viruses have tried to infect, so that the final $\psi^I(m) = \psi^I_N(m)$. The process starts with $\psi^I_{k=0}(m) = \psi^R(m)$, the viruses remaining in the cells after the previous iteration (previous time step), and the first virus is represented by $k = 1$.

This process assumes an integer number of viruses N, but the results of the previous iteration (reproduction and mutation process) yield a real number. To obtain an integer number of viruses we interpolate to the nearest integer and define this as N.

4.3.3 Administering Anti-viral Therapeutics

For viral fecundity and reproduction, there is only one parameter affecting the probability of viral success (in our model), and we multiply the respective probability prior to administering the antiviral by a prefactor representing dosage of the therapeutic, F and R. For therapeutics affecting infection, of the two factors that impact viral infection in our model, cell permissivity and cell occupancy, only cell permissivity is modified. Therefore, we do not multiply the entire infective addition of each kth virus by the inhibition of the therapeutic I, but rather just that part involved in cell permissivity, $e_m = exp(\frac{-(50-m)}{T})$. We write $e_{m(infect)}$ in the equation for infection above, to show where it appears. The equations representing the application of the therapeutics for each of the three strategies considered in this paper are shown below.

$$
\begin{aligned}
e_{m(infect)} &= I\ e_m \\
e_{m(repro)} &= R\ e_m \\
f_{therapeutic} &= F\ f \\
N &= F\ cf \sum_m \psi^F(m)
\end{aligned}
$$

Here I, R, and F are all between 1 (no therapeutic) and 0. The last equation shows how the number of viruses, N, in the bloodstream for the next iteration is obtained, where f is the fecundity. Note that N above is the expectation value of the number of viruses, and hence a real number. This is rounded to the nearest integer for the infection process, where k must run from 1 to N.

4.3.4 Meaning of extinction and time in the model

Here we are going to elaborate the definition of extinction values and time. In our model, we assumed that the virus is extinct when the virus population in the bloodstream reduces to a number less than 0.1. Regarding time in the paper, one time unit means one viral life cycle calculation. In a real life scenario, this could be between half-a-day and a day, depending on the specific viral type [55] Below we show the evolution viral population with time in the bloodstream and inside cells for the three antiviral strategies discussed in the paper.

4.3.5 Targeting Fecundity (Details)

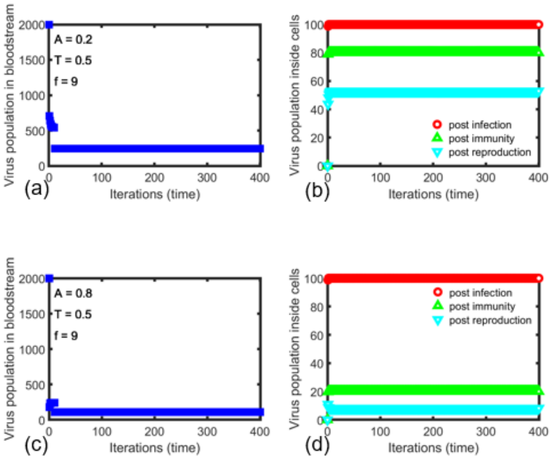

Figure 4.7: Virus Population in the bloodstream and inside cells for f=9. The therapeutics applied reduces fecundity to 9 after 10th iteration. Top row corresponds to low immunity and bottom row to high immunity.

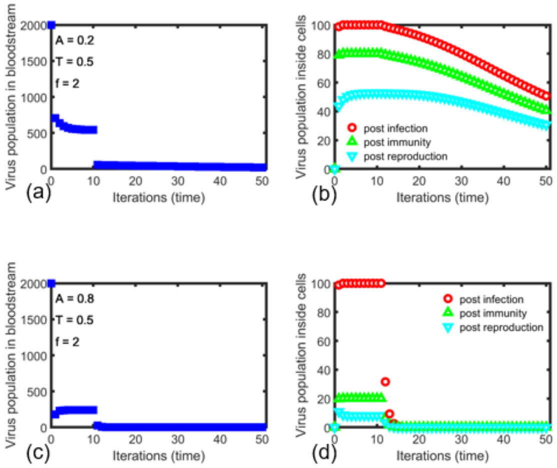

Figure 4.8: Virus Population in the bloodstream and inside cells. The therapeutics applied reduces fecundity to 2 after 10th iteration. Top row corresponds to low immunity and bottom row to high immunity..

4.3.6 Targeting Reproduction Rate (Details)

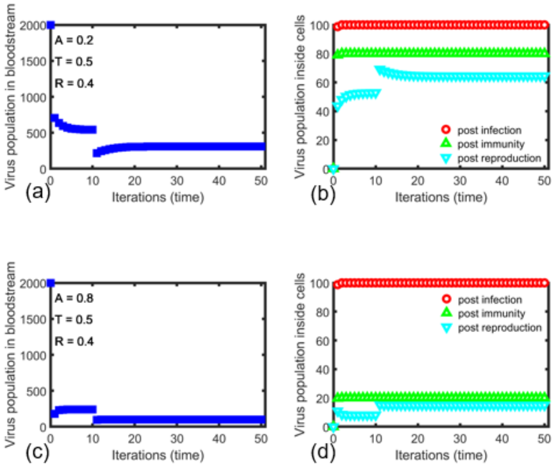

Figure 4.9: Virus Population in the bloodstream and inside cells. The therapeutics applied reduces reproduction rate R to 0.4 after 10th iteration. Top row corresponds to low immunity and bottom row to high immunity.

4.3.7 Targeting Infection Rate (Details)

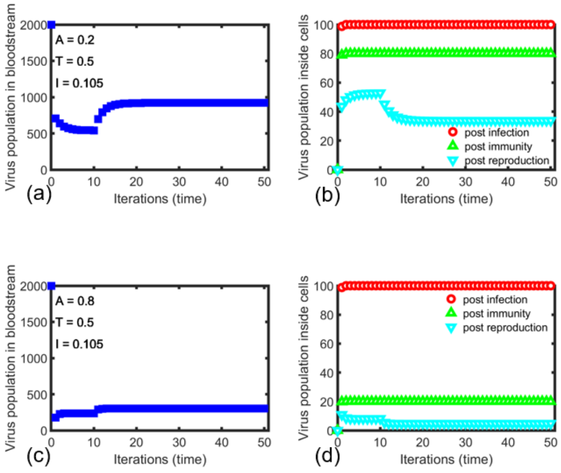

Figure 4.10: Virus Population in the bloodstream and inside cells. The therapeutics applied reduces infection rate I to 0.105 after 10th iteration. Top row corresponds to low immunity and bottom row to high immunity.

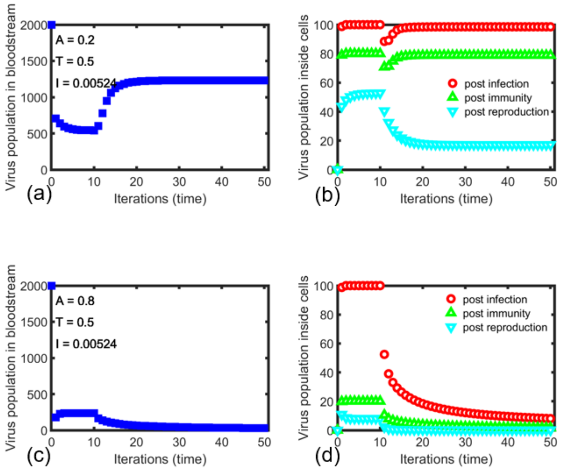

Figure 4.11: Virus Population in the bloodstream and inside cells. The therapeutics applied reduces infection rate I to 0.00524 after 10th iteration. Top row corresponds to low immunity and bottom row to high immunity.

Chapter 5

Conclusion

5.1 Conclusion

In his book *What is life?*, Schrodinger argued that the functioning of an organism is dependent on precise physical laws [81]. Understanding these laws in the complex and dynamic environment of biological systems has been a major challenge for humanity. However, this pursuit is critical for understanding the rules of life and harnessing them for developing materials that might benefit humanity and our planet, and for discovering potential treatments for various diseases. As a small step towards this, we applied the principles of statistical physics to model three biological systems: cells, tissues, and viruses. In the first project, we demonstrated how a double-network filamentous system can achieve tunable mechanics and fracture resistance. In the second project, we explained how rigidity and contractility emerge in a reconstituted active cytoskeletal composite. Finally, we analyzed the effectiveness of antivirals that disrupt three different stages of the viral lifecycle - fecundity, reproduction rate, and infection rate - to gain insight into the comparative efficacy of these drugs.

Our work shows how statistical physics based models can be used to understand the mechanistic rules and principles that underlie collective properties of complex biological systems. By developing microscopic models of cells, tissues, and viruses, we were able to gain insights into their emergent behavior under conditions of health and disease. Our findings could have implications in the design of new therapeutics and materials for a range of biological applications. As we continue to explore the physical laws governing biological systems, we move closer to unraveling the mysteries of life and its intricate workings.

Chapter 6

Future Work

6.1 Future Work I - Viscoelasticity of RPDN Model

We note here that we can include and explore additional tuning parameters such as non-linear elasticity, viscous dissipation, structural correlations, network hierarchy, network polarization or bond polydispersity in one or both of the networks of the double network. The results presented are important in understanding how biological tissues work and also highlight the design principles for the synthetic material, which is tunable and resists cracks. Therefore, this flexibility in resulting material properties and ease of implementation not only explains the health and diseased articular cartilage tissue but also makes double networks a very attractive platform for the fabrication of mechanically tunable artificial tissue constructs. Among all these possible future steps, we would like to understand more about the role of viscous forces in the viscoelastic gel-like cartilage tissue.

Tissues like articular cartilage are known for their water content and viscoelasticity. Viscoelastic materials show not only the elastic behavior of solids but also the viscous behavior of fluid. Tissue-scale viscoelasticity is vital in both healthy and diseased biological systems, given the example of tissue folding and wound healing. In healthy tissue, especially during the early stage of embryonic development, they maintain their mechanical integrity in a short time scale while changing shape due to the viscous dissipation in a long term [73]. For example, rigidity percolation theory and the phase transition in zebrafish embryonic tissue are researched using the cell connectivity network [74]. Moreover, vertex, Voronoi, and cellular Potts models have been used to explain rheological transitions in tissues [4, 34, 40, 94]. Our model of Rigidly Percolating Double Network (RPDN) with Langevin Dynamics brings new and interesting insights to the existing mathematical models of tissues, in terms of time-varying viscous dissipation dynamics.

This work centers around the mechanics and dynamics of tissues in both healthy and diseased stages using the framework called Rigidly Percolating Double Network (RPDN). In the past and in literature, there are different studies and reports on how the OA disease changed the viscoelastic behavior of the cartilage [21]. In other words, understanding how the change in collagen or aggrecan results in the temporal change in viscosity is important. Moreover, the degraded tissue is found to be responding differently to large-strain shear [58].

6.2 Future Work II - Wound Healing Mechanism in Stentor Modeling

Stentor coeruleus is best known for its many properties, including its regenerative and wound healing properties [85]. Found in the water of the pond as a trumpet-shaped ciliated single-cellular organism, it is also recognized for its reorganized and coordinated movements [97]. Among all these amazing biological capabilities of Stentor, wound healing is the most researched topic of Stentor. Some research points out that large-scale mechanical behaviors are vital in wound repair [103]. And other genomic studies suggest that the microtubule cytoskeleton is an important piece in the process of patching over a wound in Stentor [3]. Extending our RPDN framework, our lab is planning to study the modeling aspects of the regenerative property of Stentor.

6.3 Future Work III - Living Biotic-Abiotic Materials with Temporally Programmable Actuation

Our lab recently had an opportunity to join the research work on biotic-abiotic materials with the aim of creating motion and force combining biological cells with a 3D printed synthethic hydrogel. The resulting next-generation material will act as a gap-closing microactuator timed by a biomolecular circuitry [23]. In this project, our dynamic actin-myosin-micotubule system can give some estimates on the force being generated at the boundary of the synthetic hydrogel and the active biopolymer living system.

In the above work we were only able to access the final contracted states of the the actin-myosin-microtubule system. In future work we will study the approach to these states by investigating the active Langevin dynamics of this system as shown below. In the future, this will also allow us to study the full spatiotemporal properties of the system and compare the results of the simulation with DDM and SIA analysis done on the experimental data. The preliminary results are shown in Figs. 6.3, 6.2.

$$\gamma \frac{dx}{dt} = -\frac{dE(x)}{dx} + \chi$$

$$\gamma \frac{dy}{dt} = -\frac{dE(y)}{dy} + \chi$$

Using an explicit Euler algorithm,

$$x(t+\Delta t) = x(t) + \frac{D}{k_B T} f(x(t))\Delta t + \sqrt{2D\Delta t} \quad \xi_x$$

$$y(t+\Delta t) = y(t) + \frac{D}{k_B T} f(y(t))\Delta t + \sqrt{2D\Delta t} \quad \xi_y$$

Non-dimensionalizing the equation,

$$\tilde{x}(\tilde{t}+\Delta\tilde{t}) = \tilde{x}(\tilde{t}) + f(\tilde{x}(\tilde{t}))\Delta\tilde{t} + \alpha\sqrt{2\Delta\tilde{t}} \quad \xi_x$$

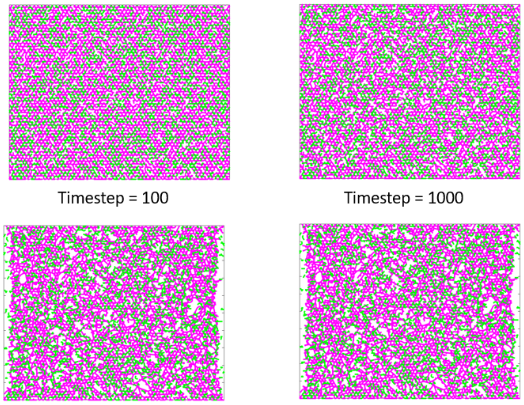

Figure 6.1: The time progression of the contractility produced inside actin-microtubule networks when $\phi_A = 0.75$ and $c_M = 0.48$.

$$\tilde{y}(\tilde{t} + \Delta\tilde{t}) = \tilde{y}(\tilde{t}) + f(\tilde{y}(\tilde{t}))\Delta\tilde{t} + \alpha\sqrt{2\Delta\tilde{t}} \quad \xi_y$$

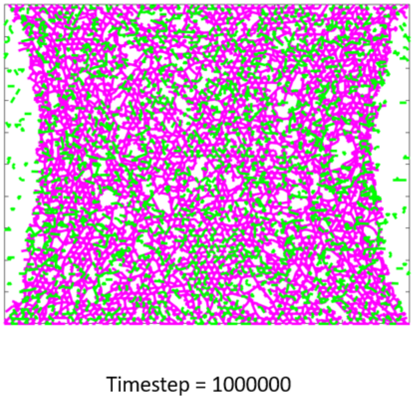

Figure 6.2: Model of an active double-network with molar actin fraction $\phi_A = 0.75$. Time evolution results is reaching the similar steady state as the previous results.

6.4 Future Work IV - Virus Modeling

Current virus modeling can be improved in some different ways. First of all, the administration of the antiviral once in the simulation can be changed into multiple doses of the antiviral. Moreover, we can also simulate the combined effect of antivirals, for example, in addition to a comparative analysis of three different types of antivirals, we can simulate the combination therapy of three types of antivirals. Last but not least, we could incorporate a better modeling of the immunity.

Chapter 7

Acknowledgements

This research was funded by several awards, including DMR-2118449, CBET-1604712, and the W.M. Keck Foundation. The models I developed were informed by discussions and experimental inputs from the collaborations these grants have funded. For computational and scientific literature resources, this work utilized services provided by RIT Research Computing and RIT library.

I would like to express my gratitude to my advisor, Dr. Moumita Das, my internship advisor, Dr. Barbara A. Jones, the rest of the dissertation committee members, the Mathematical Modeling PhD Program Faculty, the National Science Foundation, our collaborators, and RIT Research Computing, as well as Andrew B. Sindermann and Leo Sutter for their preliminary work and Dr. Jonathan Michel for valuable discussions. I would also like to thank the students in the Das Research Group, as well as my family and friends.

I would like to acknowledge the following individuals in detail. First and foremost, my parents, U./Mr. Thein Lwin and Daw./Mrs. Tin Tin Win, who instilled in me a forward-thinking mindset and encouraged me to pursue ambitious educational goals, as well as my dear Uncle U./Mr. Win Htein, who fostered my intellectual curiosity and supported my dream of studying abroad by providing me access to his library and buying my first flight ticket to America.

Completing this dissertation has been a long journey, and it reminds me of my late family members who passed away and were unable to see me graduate. I draw inspiration from the perseverance and resilience of my late grandma, Phwar Aye/ Grandma Aye, every time I face challenges in my research work. The unconditional love and unwavering support of my late uncle U./Mr. Thet Oo reminds me to carry on and keep my head held high. My witty younger sister, May-Zune, who left us during my middle school years, would have been proud to see her studious older sister earn a doctorate.

In addition to my Burmese family members, I am grateful to the family members I have gained during my ten years in America. First and foremost, my fiancé, Skylar Munger, has been by my side during the arduous final stretch of my PhD, and our outdoor activities, such as hiking, canoeing, and running, have helped build my work-life balance. I also owe thanks to other members of the Munger household, including Paul, and Kira.

Also, I would like to express my heartfelt gratitude to my friends from Hawai'i, California, Connecticut, Florida and Arizona, who know exactly who they are. You have always been there for me, lending an ear to my struggles and rejoicing in my victories. Without your support, I would not have been able to complete my PhD. Most importantly, the families in Hawai'i made my initial years in the USA smooth and welcoming. Back home, we used to have family gatherings during holidays such as Thingyan and Thadingyut. Unfortunately, I haven't been able to go home for the last ten years. However, I found an equivalent amount of joy and warmth in the Thanksgiving gatherings in the USA. I would like to thank all the families who welcomed me to their Thanksgiving and Christmas meals. And to my friends from Rochester, you have always been there for me when I needed to cook meals to de-stress, and you have always tolerated my cooking mishaps. Lastly, I want to express my deepest gratitude to my friend, Dr. Alejandro Nieto Ramos, for his invaluable guidance and unwavering friendship during the most challenging times of our PhDs.

Ultimately, I would like to dedicate my research to the young teenagers in Myanmar who aspired to become scientists but were unable to pursue their dreams due to various reasons, including the ongoing revolt against the current ruthless dictator.

* To address a grown person older than oneself, a Burmese person would use **U** for adult males and **Daw** for adult females. by Etiquette in Myanmar Wikipedia.

Chapter 8

Glossary

Glossary

contraction parameter is a parameter for actomyosin network, which leads to increasingly reduced rest lengths with an increase in myosin concentration. 58

extensibility or the strain corresponding to the peak stress is the maximum amount of deformation that the material can undergo before it fractures. It is a critical parameter because it determines the maximum amount of deformation that the material can withstand before failing. 14, 34, 37

fecundity is the maximum number of offspring per viral infection per iteration. 16, 70, 71, 72, 74, 75, 76, 77, 78, 79, 80, 81, 82, 83, 84, 88, 89, 90, 91, 94

infection rate is the rate at which a cell is infected by a virus. 16, 70, 71, 75, 78, 79, 80, 81, 82, 83, 84, 92, 94

match number is the number of matches between cell and virus genetic sequences. 72, 73, 74, 76, 80, 82, 83, 87

peak stress determines the maximum load or stress that the material can withstand before it deforms. 28, 29, 30, 34, 35, 37, 40, 41, 45, 51, 52, 53

reproduction rate is the rate of reproduction of a virus 75, 77, 78, 79, 80, 81, 82, 83, 84, 91, 94

toughness is a measure of a material's ability to absorb energy without fracturing. It is calculated as the area under the stress-strain curve because it represents the work done on the material as it is deformed or elongated by the applied load. 13, 14, 28, 29, 30, 37, 45, 53

Chapter 9

Bibliography

Bibliography

[1] Ritonavir-boosted nirmatrelvir. *(NIH website)*, 2022. URL https://www.covid19treatmentguidelines.nih.gov/therapies/antiviral-therapy/ritonavir-boosted-nirmatrelvir--paxlovid-/.

[2] Fda updates on paxlovid for health care providers. *Food and Drug Administration (FDA)*, 2022. URL https://www.fda.gov/drugs/news-events-human-drugs/fda-updates-paxlovid-health-care-providers.

[3] A. R. Albright, D. Angeles-Albores, and W. F. Marshall. Genome wide-analysis of anterior-posterior mrna localization in stentor coeruleus reveals a role for the microtubule cytoskeleton. *bioRxiv*, pages 2023–01, 2023.

[4] S. Alt, P. Ganguly, and G. Salbreux. Vertex models: from cell mechanics to tissue morphogenesis. *Philosophical Transactions of the Royal Society B: Biological Sciences*, 372(1720):20150520, 2017.

[5] C. Broedersz and F. MacKintosh. Molecular motors stiffen non-affine semiflexible polymer networks. *Soft Matter*, 7(7):3186–3191, 2011.

[6] C. Broedersz, X. Mao, T. Lubensky, and F. C. MacKintosh. Criticality and isostaticity in fibre networks. *Nature Phys.*, 7:983–988, 2011. doi: 10.1038/nphys2127.

[7] F. Burla, J. Tauber, S. Dussi, J. van der Gucht, and G. H. Koenderink. Stress management in composite biopolymer networks. *Nature Physics*, 15(6):549–553, 2019. doi: 10.1038/s41567-019-0443-6. URL `https://doi.org/10.1038/s41567-019-0443-6`.

[8] F. Burla, S. Dussi, C. Martinez-Torres, J. Tauber, J. van der Gucht, and G. H. Koenderink. Connectivity and plasticity determine collagen network fracture. *Proceedings of the National Academy of Sciences*, 117(15):8326–8334, 2020. doi: 10.1073/pnas.1920062117.

[9] L. Caly, J. D. Druce, M. G. Catton, D. A. Jans, and K. M. Wagstaff. The fda-approved drug ivermectin inhibits the replication of sars-cov-2 in vitro. *Antiviral research*, 178:104787, 2020.

[10] L. Canini and A. S. Perelson. Viral kinetic modeling: state of the art. *Journal of pharmacokinetics and pharmacodynamics*, 41(5):431–443, 2014.

[11] S. Capponi, S. Wang, E. J. Navarro, and S. Bianco. Ai-driven prediction of sars-cov-2 variant binding trends from atomistic simulations. *The European Physical Journal E*, 44(10):1–17, 2021.

[12] J. Cepelewicz and s. Quanta Magazine moderates comments tonbsp;facilitate an informed. Seeing emergent physics behind evolution.

Quanta Magazine, Sep 2017. URL https://www.quantamagazine.org/seeing-emergent-physics-behind-evolution-20170831/.

[13] E. Chigutsa, L. O'Brien, L. Ferguson-Sells, A. Long, and J. Chien. Population pharmacokinetics and pharmacodynamics of the neutralizing antibodies bamlanivimab and etesevimab in patients with mild to moderate covid-19 infection. *Clinical Pharmacology & Therapeutics*, 110(5):1302–1310, 2021.

[14] S. Chowdhury, J. Chowdhury, S. F. Ahmed, P. Agarwal, I. A. Badruddin, and S. Kamangar. Mathematical modelling of covid-19 disease dynamics: Interaction between immune system and sars-cov-2 within host. *AIMS Mathematics*, 7(2):2618–2633, 2022.

[15] J. Couzin-Frankel. Clues to long covid. *Science*, 376(6599):1261–5, 2022.

[16] M. Das and F. C. MacKintosh. Poisson's ratio in composite elastic media with rigid rods. *Phys. Rev. Lett.*, 105:138102, Sep 2010. doi: 10.1103/PhysRevLett.105.138102. URL https://link.aps.org/doi/10.1103/PhysRevLett.105.138102.

[17] M. Das, F. C. Mackintosh, and A. J. Levine. Effective medium theory of semiflexible filamentous networks. *Phys. Rev. Lett.*, 99:038101–1, 2007.

[18] M. Das, A. J. Levine, and F. C. Mackintosh. Bending and force propagation along intracellular microtubules. *Europhys. Lett.*, 84:18003–1, 2008.

[19] M. Das, D. A. Quint, and J. M. Schwarz. Redundancy and cooperativity in

the mechanics of compositely crosslinked filamentous networks. *PLoS ONE*, 7: e35939–1–11, 2012. doi: 10.1371/journal.pone.0035939.

[20] R. Desikan, P. Padmanabhan, A. M. Kierzek, and P. H. van der Graaf. Mechanistic models of covid-19: Insights into disease progression, vaccines, and therapeutics. *International Journal of Antimicrobial Agents*, page 106606, 2022.

[21] J. Desrochers, M. Amrein, and J. Matyas. Viscoelasticity of the articular cartilage surface in early osteoarthritis. *Osteoarthritis and cartilage*, 20(5): 413–421, 2012.

[22] R. Dijkgraaf and s. Quanta Magazine moderates comments tonbsp;facilitate an informed. To solve the biggest mystery in physics, join two kinds of law. *Quanta Magazine*, Sep 2017. URL `https://www.quantamagazine.org/to-solve-the-biggest-mystery-in-physics-join-two-kinds-of-law-20170907/`.

[23] DMREF. Living biotic-abiotic materials with temporally programmable actuation.

[24] L. Farhadi, S. N. Ricketts, M. J. Rust, M. Das, R. M. Robertson-Anderson, and J. L. Ross. Actin and microtubule crosslinkers tune mobility and control co-localization in a composite cytoskeletal network. *Soft Matter*, pages –, 2020. doi: 10.1039/C9SM02400J. URL `http://dx.doi.org/10.1039/C9SM02400J`.

[25] S. Feng, M. F. Thorpe, and E. Garboczi. Effective-medium theory of percolation on central-force elastic networks. *Phys. Rev. B*, 31:276–280, Jan 1985.

doi: 10.1103/PhysRevB.31.276. URL https://link.aps.org/doi/10.1103/PhysRevB.31.276.

[26] P. C. Foster, N. J. Mlot, A. Lin, and D. L. Hu. Fire ants actively control spacing and orientation within self-assemblages. *Journal of Experimental Biology*, 217 (12):2089–2100, 2014.

[27] M. L. Francis, S. N. Ricketts, L. Farhadi, M. J. Rust, M. Das, J. L. Ross, and R. M. Robertson-Anderson. Non-monotonic dependence of stiffness on actin crosslinking in cytoskeleton composites. *Soft Matter*, 15(44):9056–9065, 2019.

[28] A. Frediansyah, R. Tiwari, K. Sharun, K. Dhama, and H. Harapan. Antivirals for covid-19: A critical review. *Clinical Epidemiology and Global Health*, 9: 90–98, 2021. ISSN 2213-3984.

[29] Y. Fung. *Biomechanics: Mechanical Properties of Living Tissues*. Springer-Verlag, New York, 2 edition, 1993.

[30] M. Gardel, J. Shin, F. MacKintosh, L. Mahadevan, P. Matsudaira, and D. Weitz. Scaling of f-actin network rheology to probe single filament elasticity and dynamics. *Physical review letters*, 93(18):188102, 2004.

[31] F. Graw and A. S. Perelson. Modeling viral spread. *Annual review of virology*, 3(1):555, 2016.

[32] D. J. Griffin, J. Vicari, M. R. Buckley, J. L. Silverberg, I. Cohen, and L. J. Bonassar. Effects of enzymatic treatments on the depth-dependent viscoelastic shear properties of articular cartilage. *Journal of Orthopaedic Research*, 32

(12):1652–1657, 2014. doi: 10.1002/jor.22713. URL https://onlinelibrary.wiley.com/doi/abs/10.1002/jor.22713.

[33] J. Guedj, J. Yu, M. Levi, B. Li, S. Kern, N. V. Naoumov, and A. S. Perelson. Modeling viral kinetics and treatment outcome during alisporivir interferon-free treatment in hepatitis c virus genotype 2 and 3 patients. *Hepatology*, 59 (5):1706–1714, 2014.

[34] E. Hannezo and C.-P. Heisenberg. Rigidity transitions in development and disease. *Trends in Cell Biology*, 2022.

[35] M. A. Haque, T. Kurokawa, and J. P. Gong. Super tough double network hydrogels and their application as biomaterials. *Polymer*, 53:1805–1822, 2012.

[36] D. A. Head, A. J. Levine, and F. C. MacKintosh. Distinct regimes of elastic response and deformation modes of cross-linked cytoskeletal and semiflexible polymer networks. *Phys. Rev. E*, 68:061907–1–14, 2003. doi: 10.1103/PhysRevE.68.061907.

[37] F. Heidary and R. Gharebaghi. Ivermectin: a systematic review from antiviral effects to covid-19 complementary regimen. *The Journal of antibiotics*, 73(9): 593–602, 2020.

[38] E. A. Hernandez-Vargas and J. X. Velasco-Hernandez. In-host mathematical modelling of covid-19 in humans. *Annual reviews in control*, 50:448–456, 2020.

[39] C. Heussinger and E. Frey. Floppy modes and nonaffine deformations in random fiber networks. *Phys. Rev. Lett.*, 97:105501–1, 2006.

[40] H. Honda, M. Tanemura, and T. Nagai. A three-dimensional vertex dynamics cell model of space-filling polyhedra simulating cell behavior in a cell aggregate. *Journal of theoretical biology*, 226(4):439–453, 2004.

[41] M. Hussein, B. Berkhout, and E. Herrera-Carrillo. Crispr-cas-based gene therapy to target viral infections. *Biotechnologies for Gene Therapy: RNA, CRISPR, Nanobots, and Preclinical Applications*, page 85.

[42] B. A. Jones, J. Lessler, S. Bianco, and J. H. Kaufman. Statistical mechanics and thermodynamics of viral evolution. *PloS one*, 10(9):e0137482, 2015.

[43] H. Kang, Q. Wen, P. A. Janmey, J. X. Tang, E. Conti, and F. C. MacKintosh. Nonlinear elasticity of stiff filament networks: Strain stiffening, negative normal stress, and filament alignment in fibrin gels†. *The Journal of Physical Chemistry B*, 113(12):3799–3805, 2009.

[44] T. Karamitros, G. Papadopoulou, M. Bousali, A. Mexias, S. Tsiodras, and A. Mentis. Sars-cov-2 exhibits intra-host genomic plasticity and low-frequency polymorphic quasispecies. *Journal of Clinical Virology*, 131:104585, 2020.

[45] M. Kardar. Statistical physics of fields. 2007.

[46] M. Kardar. Statistical physics of particles. 2007.

[47] S. Kausar, F. S. Khan, M. I. M. U. Rehman, M. Akram, M. Riaz, G. Rasool, A. H. Khan, I. Saleem, S. Shamim, and A. Malik. A review: Mechanism of action of antiviral drugs. *International Journal of Immunopathology and Pharmacology*, 35:20587384211002621, 2021. doi: 10.1177/20587384211002621.

[48] J. H. Lai and M. E. Levenston. Meniscus and cartilage exhibit distinct intra-tissue strain distributions under unconfined compression. *Osteoarthritis Cartilage*, 18:1291–1299, 2010.

[49] Y. N. Lamb. Nirmatrelvir plus ritonavir: First approval. *Drugs*, pages 1–7, 2022.

[50] B. Lautrup. *Physics of continuous matter: exotic and everyday phenomena in the macroscopic world*. CRC press, 2011.

[51] H. Ledford. Long-covid treatments: why the world is still waiting. *Nature*, 608 (7922):258–260, 2022.

[52] H. Ledford et al. Covid antiviral pills: what scientists still want to know. *Nature*, 599(7885):358–359, 2021.

[53] G. Lee, G. Leech, P. Lwin, J. Michel, C. Currie, M. J. Rust, J. L. Ross, R. J. McGorty, M. Das, and R. M. Robertson-Anderson. Active cytoskeletal composites display emergent tunable contractility and restructuring. *Soft Matter*, 17(47):10765–10776, 2021.

[54] G. Lee, G. Leech, M. J. Rust, M. Das, R. J. McGorty, J. L. Ross, and R. M. Robertson-Anderson. Myosin-driven actin-microtubule networks exhibit self-organized contractile dynamics. *Science Advances*, 7(6):eabe4334, 2021.

[55] G. R. Lewis, W. F. Marshall, and B. A. Jones. Modeling the dynamics of within-host viral infection and evolution predicts quasispecies distributions and phase boundaries separating distinct classes of infections. *bioRxiv*, 2021.

[56] C. Li, Y. Zhang, and Y. Zhou. Spatially antiviral dynamics determines hcv in vivo replication and evolution. *Journal of Theoretical Biology*, 503:110378, 2020.

[57] E. Mahase. Covid-19: Pfizer's paxlovid is 89% effective in patients at risk of serious illness, company reports, 2021.

[58] F. Maier, C. Lewis, and D. Pierce. The evolving large-strain shear responses of progressively osteoarthritic human cartilage. *Osteoarthritis and Cartilage*, 27(5):810–822, 2019.

[59] X. Mao, O. Stenull, and T. C. Lubensky. Elasticity of a filamentous kagome lattice. *Phys. Rev. E*, 87:042602, Apr 2013. doi: 10.1103/PhysRevE.87.042602. URL `https://link.aps.org/doi/10.1103/PhysRevE.87.042602`.

[60] M. Marshall. The lasting misery of coronavirus long-haulers. *Nature*, 585 (7825):339–342, 2020.

[61] A. R. Missel, M. Bai, W. S. Klug, and A. J. Levine. Affine-nonaffine transitions in networks of nematically ordered semiflexible polymers. *Phys. Rev. E*, 82: 041907–1, 2010.

[62] V. C. Mow, A. Ratcliffe, and A. R. Poole. Cartilage and diarthrodial joints as paradigms for hierarchical materials and structures. *Biomaterials*, 13:67–97, 1992. doi: 10.1016/0142-9612(92)90001-5.

[63] D. S. Nedrelow, D. Bankwala, J. D. Hyypio, V. K. Lai, and V. H. Barocas.

Mechanics of a two-fiber model with one nested fiber network, as applied to the collagen-fibrin system. *Acta biomaterialia*, 72:306–315, 2018.

[64] P. Nelson, G. Reynolds, E. Waldron, E. Ward, K. Giannopoulos, and P. Murray. Demystified…: monoclonal antibodies. *Molecular pathology*, 53(3):111, 2000.

[65] T. H. T. Nguyen, F. Mentré, M. Levi, J. Yu, and J. Guedj. A pharmacokinetic–viral kinetic model describes the effect of alisporivir as monotherapy or in combination with peg-ifn on hepatitis c virologic response. *Clinical Pharmacology & Therapeutics*, 96(5):599–608, 2014.

[66] T. Nonoyama and J. P. Gong. Double-network hydrogel and its potential biomedical application: A review. *Polymer*, 229:853–863, 2015.

[67] S. W. O'Driscoll. The healing and regeneration of articular cartilage. *J. Bone Joint Surg. Am.*, 80:1795–1812, 1998.

[68] R. Pathria and P. D. Beale. 1-the statistical basis of thermodynamics. *Statistical Mechanics*, pages 1–23, 2011.

[69] V. Pelletier, N. Gal, P. Fournier, and M. L. Kilfoil. Microrheology of microtubule solutions and actin-microtubule composite networks. *Phys. Rev. Lett.*, 102:188303, May 2009. doi: 10.1103/PhysRevLett.102.188303. URL https://link.aps.org/doi/10.1103/PhysRevLett.102.188303.

[70] C. Perales and E. Domingo. Antiviral strategies based on lethal mutagenesis and error threshold. *Quasispecies: From Theory to Experimental Systems*, pages 323–339, 2015.

[71] A. S. Perelson and R. Ke. Mechanistic modeling of sars-cov-2 and other infectious diseases and the effects of therapeutics. *Clinical Pharmacology & Therapeutics*, 109(4):829–840, 2021.

[72] A. S. Perelson, A. U. Neumann, M. Markowitz, J. M. Leonard, and D. D. Ho. Hiv-1 dynamics in vivo: virion clearance rate, infected cell life-span, and viral generation time. *Science*, 271(5255):1582–1586, 1996.

[73] N. I. Petridou and C.-P. Heisenberg. Tissue rheology in embryonic organization. *The EMBO journal*, 38(20):e102497, 2019.

[74] N. I. Petridou, B. Corominas-Murtra, C.-P. Heisenberg, and E. Hannezo. Rigidity percolation uncovers a structural basis for embryonic tissue phase transitions. *Cell*, 184(7):1914–1928, 2021.

[75] R. C. Picu. Mechanics of random fiber networks - a review. *Soft Matter*, 7: 6768–6785, 2011. doi: 10.1039/C1SM05022B.

[76] T. D. Pollard and G. R. D., editors. *The Cytoskeleton.* Cold Spring Harbor Laboratory Press, 2017.

[77] W. H. Press, S. A. Teukolsky, W. T. Vetterling, and B. P. Flannery. *Numerical Recipes in Fortran 90: The Art of Scientific Computing, Second Edition.* Cambridge University Press, 1996.

[78] R. Pretorius. Could microclots help explain the mystery of long covid? *The Guardian*, 2022.

[79] S. N. Ricketts, J. L. Ross, and R. M. Robertson-Anderson. Co-entangled actin-microtubule composites exhibit tunable stiffness and power-law stress relaxation. *Biophysical journal*, 115(6):1055–1067, 2018.

[80] S. N. Ricketts, M. L. Francis, L. Farhadi, M. J. Rust, M. Das, J. L. Ross, and R. M. Robertson-Anderson. Varying crosslinking motifs drive the mesoscale mechanics of actin-microtubule composites. *Scientific reports*, 9(1):1–12, 2019.

[81] E. Schrodinger. *What is life? The physical aspect of the living cell.* At the University Press, 1951.

[82] M. Sheinman, C. P. Broedersz, and F. C. MacKintosh. Nonlinear effective-medium theory of disordered spring networks. *Phys. Rev. E*, 85:021801–1, 2012.

[83] Y. Si, Y. Tan, L. Gao, R. Li, C. Zhang, H. Gao, and X. Zhang. Mechanical properties of cracked articular cartilage under uniaxial creep and cyclic tensile loading. *Journal of Biomechanics*, 134:110988, 2022.

[84] J. L. Silverberg, A. R. Barrett, M. Das, P. B. Petersen, L. J. Bonassar, and I. Cohen. Structure-function relations and rigidity percolation in the shear properties of articular cartilage. *Biophysical journal*, 107(7):1721–1730, 2014.

[85] M. M. Slabodnick and W. F. Marshall. Stentor coeruleus. *Current Biology*, 24 (17):R783–R784, 2014.

[86] K. Stok and A. Oloyede. A qualitative analysis of crack propagation in articular

cartilage at varying rates of tensile loading. *Connective Tissue Research*, 44: 109–120, 2003.

[87] K. Stok and A. Oloyede. A qualitative analysis of crack propagation in articular cartilage at varying rates of tensile loading. *Connective tissue research*, 44(2): 109–120, 2003.

[88] J. Tauber, S. Dussi, and J. Van Der Gucht. Microscopic insights into the failure of elastic double networks. *Physical Review Materials*, 4(6):063603, 2020.

[89] D. Taylor, N. O'Mara, E. Ryan, M. Takaza, and C. Simms. The fracture toughness of soft tissues. *Journal of the mechanical behavior of biomedical materials*, 6:139–147, 2012.

[90] P. C. Taylor, A. C. Adams, M. M. Hufford, I. De La Torre, K. Winthrop, and R. L. Gottlieb. Neutralizing monoclonal antibodies for treatment of covid-19. *Nature Reviews Immunology*, 21(6):382–393, 2021.

[91] E. P. Tchesnokov, J. Y. Feng, D. P. Porter, and M. Götte. Mechanism of inhibition of ebola virus rna-dependent rna polymerase by remdesivir. *Viruses*, 11(4):326, 2019.

[92] D. R. Tompa, A. Immanuel, S. Srikanth, and S. Kadhirvel. Trends and strategies to combat viral infections: A review on fda approved antiviral drugs. *International Journal of Biological Macromolecules*, 172:524–541, 2021. ISSN 0141-8130. doi: https://doi.org/10.1016/j.ijbiomac.2021.01.076. URL `https://www.sciencedirect.com/science/article/pii/S0141813021001069`.

[93] D. R. Tompa, A. Immanuel, S. Srikanth, and S. Kadhirvel. Trends and strategies to combat viral infections: A review on fda approved antiviral drugs. *International Journal of Biological Macromolecules*, 172:524–541, 2021.

[94] S. Tong, N. K. Singh, R. Sknepnek, and A. Kosmrlj. Linear viscoelastic properties of the vertex model for epithelial tissues. *arXiv preprint arXiv:2102.11181*, 2021.

[95] D. Trivedi, C. D. Rahn, W. M. Kier, and I. D. Walker. Soft robotics: Biological inspiration, state of the art, and future research. *Appl. Bion. Biomech.*, 5:99–117, 2008. doi: 10.1080/11762320802557865.

[96] K. Uzunova, E. Filipova, V. Pavlova, and T. Vekov. Insights into antiviral mechanisms of remdesivir, lopinavir/ritonavir and chloroquine/hydroxychloroquine affecting the new sars-cov-2. *Biomedicine & Pharmacotherapy*, page 110668, 2020.

[97] K. Y. Wan, S. K. Hürlimann, A. M. Fenix, R. M. McGillivary, T. Makushok, E. Burns, J. Y. Sheung, and W. F. Marshall. Reorganization of complex ciliary flows around regenerating stentor coeruleus. *Philosophical Transactions of the Royal Society B*, 375(1792):20190167, 2020.

[98] H.-c. Wang, Y.-p. Ren, Y. Qiu, J. Zheng, G.-l. Li, C.-p. Hu, T.-y. Zhou, W. Lu, and L. Li. Integrated pharmacokinetic/viral dynamic model for daclatasvir/asunaprevir in treatment of patients with genotype 1 chronic hepatitis c. *Acta Pharmacologica Sinica*, 39(1):140–153, 2018.

[99] J. Wilhelm and E. Frey. Elasticity of stiff polymer networks. *Phys. Rev. Lett.*, 68:061907–1, 2003. doi: 10.1103/PhysRevE.68.061907.

[100] C. Willyard. Could tiny blood clots cause long covid's puzzling symptoms? *Nature*, 608(7924):662–664, 2022.

[101] T. Wyse Jackson, J. Michel, P. Lwin, L. A. Fortier, M. Das, L. J. Bonassar, and I. Cohen. Structural origins of cartilage shear mechanics. *Science Advances*, 8 (6):eabk2805, 2021.

[102] Y. Xiao, P. V. Lidsky, Y. Shirogane, R. Aviner, C.-T. Wu, W. Li, W. Zheng, D. Talbot, A. Catching, G. Doitsh, et al. A defective viral genome strategy elicits broad protective immunity against respiratory viruses. *Cell*, 184(25): 6037–6051, 2021.

[103] K. S. Zhang, L. R. Blauch, W. Huang, W. F. Marshall, and S. K. Tang. Microfluidic guillotine reveals multiple timescales and mechanical modes of wound response in stentor coeruleus. *BMC biology*, 19:1–17, 2021.

[104] L. Zhang, D. Z. Rocklin, L. M. Sander, and X. Mao. Fiber networks below the isostatic point: Fracture without stress concentration. *Phys. Rev. Materials*, 1:052602, Oct 2017. doi: 10.1103/PhysRevMaterials.1.052602. URL `https://link.aps.org/doi/10.1103/PhysRevMaterials.1.052602`.